Final Report
DOE Contract DE-FC02-02ER54666

SciDAC Participation in Center for Extended MHD

Period of Performance
May 15, 2005 – May 15, 2006

Summary

We report progress and participation in the SciDAC project, Center for Extended MHD Modeling. The primary activity was participation in theory milestones regarding the large scale numerical simulation of edge localized modes, or ELMs. These activities have been detailed in quarterly progress reports to the Office of Fusion Energy Science. For completeness, they are attached and serve as the body of this Final Report.

Final Report on the OFES ELM Milestone for FY2005

September 30, 2005

D. P. Brennan[1,2], E. D. Held[3], S. E. Kruger[4], A. Y. Pankin[5], D. D. Schnack[5], and C. R. Sovinec[6]

[1]Massachusetts Institute of Technology, Cambridge, Massachusetts
[2]General Atomics, San Diego, California
[3]Utah State University, Logan, Utah
[4]Tech-X Corporation, Boulder, Colorado
[5]Science Applications International Corporation, San Diego, California
[6]University of Wisconsin, Madison, Wisconsin

NOTICE

This report was prepared as an account of work sponsored by the United States Government. Neither the United States nor the United States Department of Energy, nor any of their employees, nor any of their contractors, subcontractors, or their employees, makes any warranty, express or implied, or assumes any legal liability or responsibility for the accuracy, completeness, or usefulness of any information, apparatus, product or process disclosed or represents that its use would not infringe.

This work is supported by DOE grant numbers DE-FC02-02ER54668, DE-FC02-04ER54798, DE-FC03-02ER54666, DE-FG03-95ER54309, and DE-FG02-04ER54799. This research used resources of the National Energy Research Scientific Computing Center, which is supported by the Office of Science of the U.S. Department of Energy under Contract No. DE-AC03-76SF00098.

Final Report on the OFES ELM Milestone for FY2005

D. P. Brennan[1,2], E. D. Held[3], S. E. Kruger[4], A. Y. Pankin[5], D. D. Schnack[5], and C. R. Sovinec[6]

[1]Massachusetts Institute of Technology, Cambridge, Massachusetts
[2]General Atomics, San Diego, California
[3]Utah State University, Logan, Utah
[4]Tech-X Corporation, Boulder, Colorado
[5]Science Applications International Corporation, San Diego, California
[6]University of Wisconsin, Madison, Wisconsin

Executive summary

This document reports the successful completion of the OFES Theory Milestone for FY2005, namely, *Perform parametric studies to better understand the edge physics regimes of laboratory experiments. Simulate at increased resolution (up to 20 toroidal modes), with density evolution, late into the nonlinear phase and compare results from different types of edge modes. Simulate a single case including a study of heat deposition on nearby material walls*.

The linear stability properties and nonlinear evolution of Edge Localized Modes (ELMs) in tokamak plasmas are investigated through numerical computation. Data from the DIII-D device at General Atomics (http://fusion.gat.com/diii-d/) is used for the magnetohydrodynamic (MHD) equilibria, but edge parameters are varied to reveal important physical effects. The equilibrium with very low magnetic shear produces an unstable spectrum that is somewhat insensitive to dissipation coefficient values. Here, linear growth rates from the non-ideal NIMROD code (http://nimrodteam.org) agree reasonably well with ideal, i.e. non-dissipative, results from the GATO global linear stability code at low toroidal mode number (n) and with ideal results from the ELITE edge linear stability code at moderate to high toroidal mode number. Linear studies with a more realistic sequence of MHD equilibria (based on DIII-D discharge 86166) produce more significant discrepancies between the ideal and non-ideal calculations. The maximum growth rate for the ideal computations occurs at toroidal mode index n=10, whereas growth rates in the non-ideal computations continue to increase with n unless strong anisotropic thermal conduction is included. Recent modeling advances allow drift effects associated with the Hall electric field and gyroviscosity to be considered. A stabilizing effect can be observed in the preliminary results, but while the distortion in mode structure is readily apparent at n=40, the growth rate is only 13% less than the non-ideal MHD result. Computations performed with a non-local kinetic closure for parallel electron thermal conduction that is valid over all collisionality regimes identify thermal diffusivity ratios of $\chi_{\|}/\chi_{\perp} \sim 10^{7}-10^{8}$ as appropriate when using collisional heat flux modeling for these modes. Adding significant parallel viscosity proves to have little effect.

Nonlinear ELM computations solve the resistive MHD model with toroidal resolution $0 \le n \le 21$, including anisotropic thermal conduction, temperature-dependent resistivity, and number density evolution. The computations are based on a realistic equilibrium with high pedestal temperature from the linear study. When the simulated ELM grows to appreciable amplitude, ribbon-like thermal structures extend from the separatrix to the wall as the spectrum broadens about a peak at n=13. Analysis of the results finds the heat flux on the wall to be very nonuniform with greatest intensity occurring in spots on the top and bottom of the chamber. Net thermal energy loss occurs on a time-scale of 100 μs, and the instantaneous loss rate exceeds 1 GW.

1.0 Introduction

With recent advances in computer hardware and numerical algorithm efficiency, large-scale computational modeling can play an important role in the design and analysis of fusion devices. Among the nations engaged in developing magnetic confinement fusion, the US remains the world leader in plasma simulation. An example of an important fusion problem that is being addressed by this approach is the onset and nonlinear evolution of Edge Localized Modes (ELMs) and their effect on global confinement and first wall performance [1]. These modes shed thermal energy from the edge of the confinement region and, in their most virulent form, release enough energy to be of concern for plasma-facing components of future burning plasma experiments. They may also affect the core plasma through nonlinear mode coupling. During FY2005, the NIMROD Team (http://nimrodteam.org) has begun a numerical study of the global dynamics of ELMs in tokamaks. The unique capabilities of our advanced extended-MHD model [2] allow us to simulate ELMs farther into the nonlinear regime than what has been previously achieved.

Previous studies have found the underlying character of ELMs to be an MHD instability described as "peeling-ballooning" [3-5]. The "peeling" component of the instability is the free-energy drive due to the current density gradient, and the "ballooning" component is the free-energy drive due to the pressure gradient. At the edge of the confinement region of tokamaks, poloidal flows reduce energy transport and allow a steep pressure gradient to develop. Through bootstrap-current effects, the strong pressure gradient drives highly localized charge-current density. The pressure and current gradients are also coupled through the MHD equilibrium force-balance, but they effect distinct characteristics in the linearly unstable modes that are excited. An individual ELM will typically display a combination of both sets of characteristics, however.

Our linear stability analysis of a set of tokamak equilibria having varying degrees of peeling and ballooning drive is outlined in Section 2. A sequence of nonlinear simulations follow a spectrum of ELMs from the linear stage to finite amplitude, where they become coupled and transport heat beyond the confinement zone and to the wall. These results are presented in Section 3. A brief summary and discussion is presented in Section 4.

2.0 Linear Stability

2.1 Ballooning-component-dominant equilibria

A model tokamak equilibrium configuration has been constructed to be robustly unstable, due to low magnetic shear and poloidal shaping, while remaining in the global parameter space of typical DIII-D discharges. The localized edge current density and pressure gradient described in Section 1.0 are clearly evident in the profiles shown in Figure 1. This ballooning-dominant configuration is relatively easy to resolve radially. Consistent with the MHD theory of ballooning modes, the resistive MHD computations find that growth rates increase monotonically with n. The unfortunate implication is that toroidal resolution in a nonlinear resistive MHD simulation cannot be achieved. Nonetheless, this equilibrium provides a suitable benchmark case for comparing linear results obtained with different numerical approaches.

The linear results of NIMROD compare favorably with results from the ELITE and GATO [4] codes with eigenfunctions and growth rates that are in reasonable agreement. The growth rates computed by NIMROD with non-ideal MHD depend on the resistivity and viscosity in the vicinity of the mode, as discussed below, but the variation of growth

rate with *n* agrees qualitatively with the GATO and ELITE results, as shown in Figure 2. Varying the electrical resistivity shaping parameter by three orders of magnitude affects the growth rate values (by less than a factor of 2), but it does not change the spectrum qualitatively. Here, the magnetic Prandtl number (Pm, the ratio of kinematic viscosity to electrical diffusivity) is held fixed while both the core and surrounding resistivity values are varied. In obtaining the results for this equilibrium, the linear behavior of 22 toroidal modes have been determined with 3 values of resistivity and 3 values of thermal conductivity, for a total of 198 numerical calculations. The results represent the first linear ELM studies to include collisionality and separatrix effects.

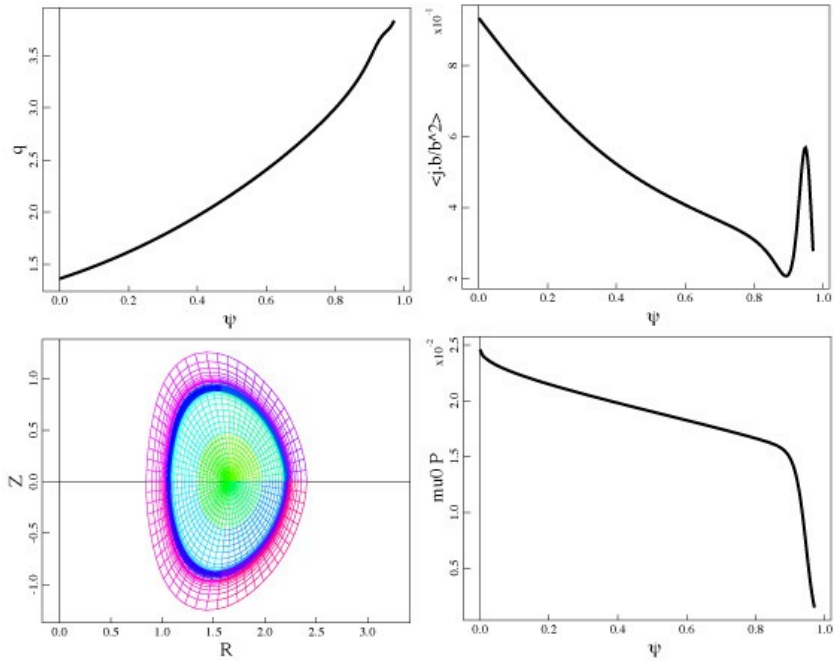

Figure 1. Safety factor (*q*), parallel charge-current density ($\mathbf{j}\cdot\mathbf{b}/\mathbf{b}^2$), and pressure profiles for the low-shear equilibrium discussed in Section 2.1. The computational mesh of finite elements used for the linear computations is also shown.

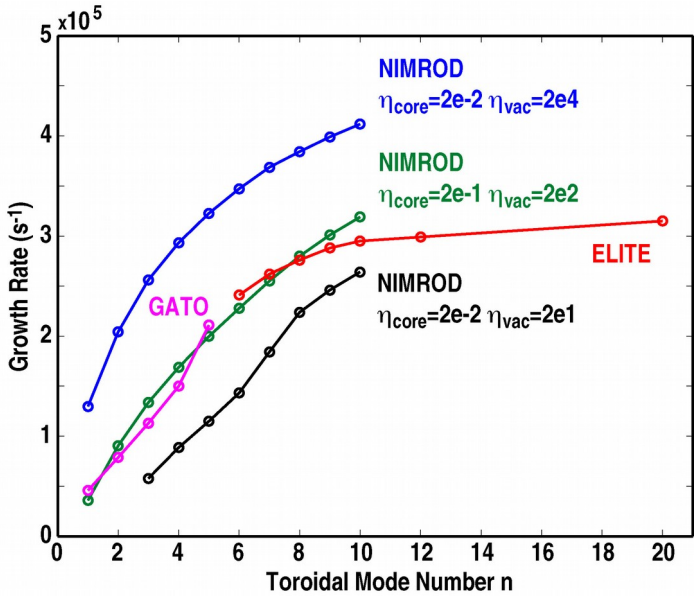

Figure 2. Linear growth rates for a range of *n*-values with confinement-region resistivity (η_{core}) and surrounding layer resistivity (η_{vac}) varied show good agreement with ideal MHD codes. Because the eigenfunctions extend into the open-field line region, the growth rates depend on the "vacuum" resistivity, but the changes are less than a factor of 2.

2.2. Realistic equilibria

Equilibria reconstructed with data from a high-pressure DIII-D discharge that produced ELMs provide the basis of this investigation. The poloidal magnetic field configuration has a single null below the confinement region. The non-dimensional geometric and profile properties are also similar to high performance tokamak operation ("H-mode") in Alcator C-mod (http://www.psfc.mit.edu) and advanced scenarios for ITER (http://www.iter.org). The parallel current density, magnetic winding ratio (or 'safety factor,' *q*), and pressure profiles for three of the equilibria are shown in Figure 3. They are parameterized by their edge pedestal temperatures (T_{ped}) with the 100 eV, 400 eV, and 700 eV profiles shown in the figure. The *q*-value is above 1 across each profile, which stabilizes the internal ideal kink mode and allows our study to focus on edge-localized modes. The equilibrium with $T_{\pi\varepsilon\delta} = 100$ ες does not have any significant gradients in the edge.

The linear stability properties of this set of equilibria have been studied with the NIMROD code with the Lundquist number (S) set to 2×10^7. The linear growth rate spectrum with respect to toroidal mode number is shown in Figure 4 for two of the equilibria. All modes for the T_{ped} = 400 eV and 700 eV cases are found to be unstable, and the growth rates of the unstable modes increase with increasing *n*. The $T_{ped} = 700$ eV computation produces large linear growth rates ($\gamma\tau_A = 0.36$, where τ_A is the global Alfvén propagation time) at low Pm-values with the non-ideal model. This indicates that the respective equilibrium is well above the threshold for ideal linear instability, a condition that is unlikely to occur in the actual experiment. The T_{ped} = 100 eV equilibrium is near the stability boundary.

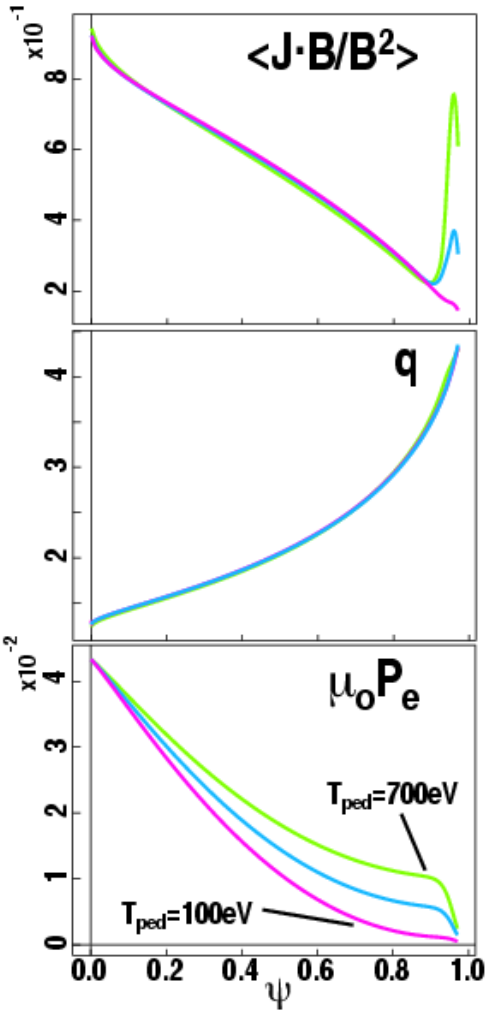

Figure 3. MHD equilibria representative of DIII-D with successively decreasing pedestal temperature but similar cross sectional shape. The top figure shows the parallel current profiles, the middle figure shows the *q*-profiles, and the bottom figure shows the temperature.

Resistive MHD produces growth rates that increase with *n* for ballooning-dominant equilibria, but high-*n* ELM fluctuations are not detected in experiments. Conventional wisdom holds that two-fluid effects are stabilizing at large *n*-values, and this is often cited to explain the observations. We have applied extended MHD modeling [6] to the equilibria shown in Figure 3 (also see Ref. [5]), and preliminary results for the T_{ped} = 400 eV equilibrium are summarized in Figure 5. Here we plot the linear growth rate as a function of the toroidal mode number for three different models (MHD, Hall-MHD, and Hall-MHD with gyroviscosity) with and without anisotropic ($\chi_{\parallel}/\chi_{\perp}=10^{7}$) thermal diffusivity. The strongest stabilizing effect is provided by the anisotropic thermal diffusivity, where the ratio of diffusivity coefficients has been determined by computations performed with a non-local kinetic closure for parallel electron thermal conduction that is valid over all collisionality regimes [7]. A linear computation for the T_{ped} = 700 eV equilibrium without anisotropic thermal conduction finds only a 13% reduction in growth rate when Hall and gyroviscous effects are included at *n*=40.

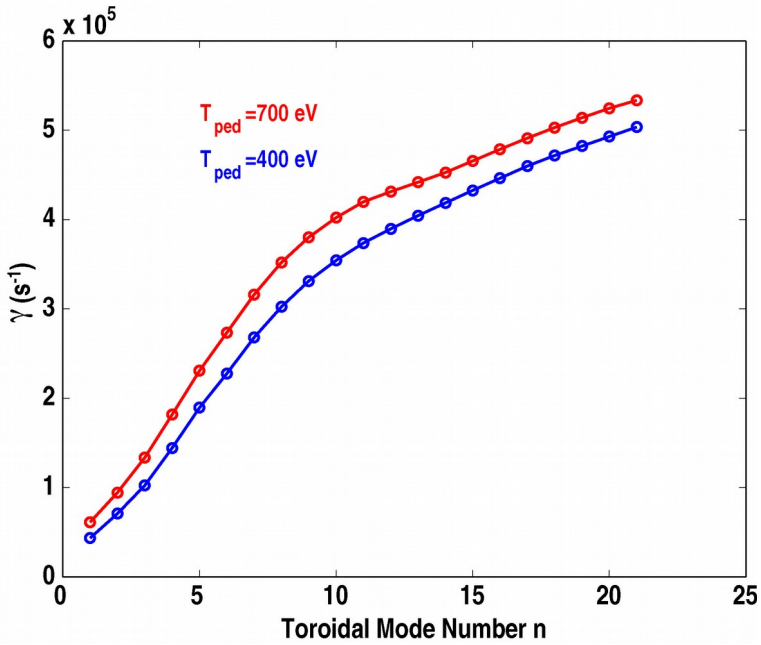

Figure 4. Linear growth rates as a function of toroidal mode index *n* for the equilibria with pedestal temperatures of 400 eV (blue trace) and 700 eV (red trace). The 100eV equilibrium is near the stability threshold.

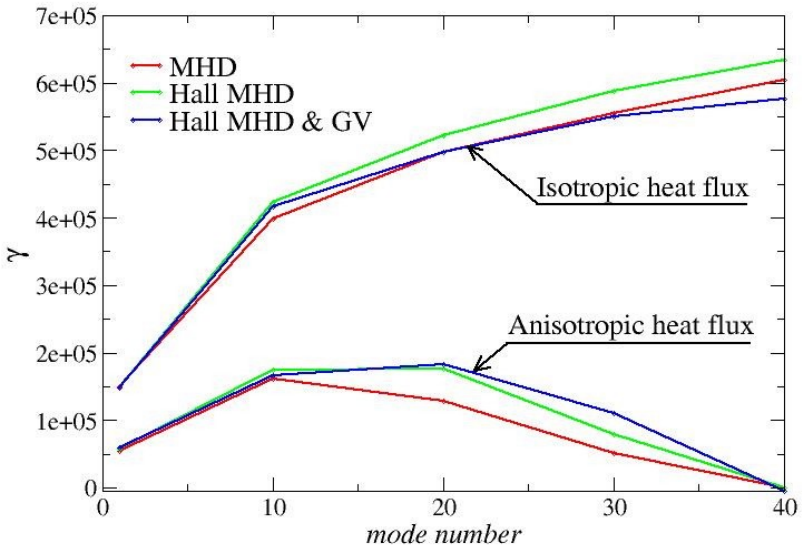

Figure 5. Linear growth rate as a function of toroidal mode number for the case of 400 eV pedestal temperature, $S = 3.7\times10^{7}$, $Pm = 10^{-3}$.

3.0 Nonlinear Resistive MHD

Nonlinear, resistive MHD simulations with anisotropic heat conduction have been performed with several of the equilibria discussed above. Here, we present a computation that is based on the T_{ped}=700 eV equilibrium shown in Figure 3. Small amplitude perturbations in the initial conditions excite unstable ELMs, and the computation follows their evolution well into the nonlinear phase. The electrical resistivity is temperature-dependent (Spitzer resistivity, based on the evolving toroidally averaged temperature). The viscous diffusivity and perpendicular thermal diffusivity are 25 m^2/s, and the parallel thermal diffusivity is 10^5 times larger. The spatial domain is represented by an appropriately packed 40×72 mesh of biquartic finite elements for the poloidal plane and Fourier components $0 \le n \le 21$ for the toroidal direction.

The temporal evolution of the kinetic energy associated with each of the toroidal Fourier components is shown in Figure 6. There is a linear growth phase for 0.05 ms < t < 0.1 ms, followed by nonlinear saturation. Only modes in the range $7 \le \nu \le 19$ exhibit linear growth, as shown in Figure 7. In contrast to the results shown in Figure 4, the growth rate spectrum is peaked around $\nu = 13$. This is attributed to the anisotropic thermal conduction (see Figure 5), viscous dissipation, and the large current-gradient (peeling component) at the edge of the confinement region in this equilibrium. Numerical convergence tests indicate that while greater resolution is needed to achieve quantitative accuracy, the peaked linear spectrum is qualitatively correct. Other modes may be linearly unstable but grow too slowly to show independent activity before nonlinear coupling becomes significant. Of particular importance is that the nonlinear coupling drives low n-fluctuations (including n=1), in addition to high-n fluctuations, and low-n activity in the edge may excite resonant effects in the core plasma.

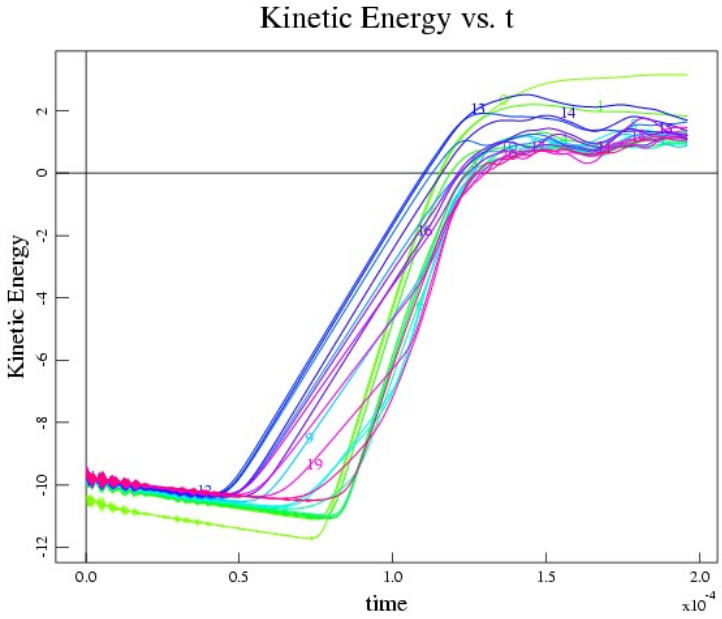

Figure 6. The evolution of kinetic fluctuation energy (on a logarithmic scale) of each toroidal harmonic shows that the broad linear mode spectrum nonlinearly drives the linearly stable n=0 and n=1 components. They have the largest energies at the end of the simulation.

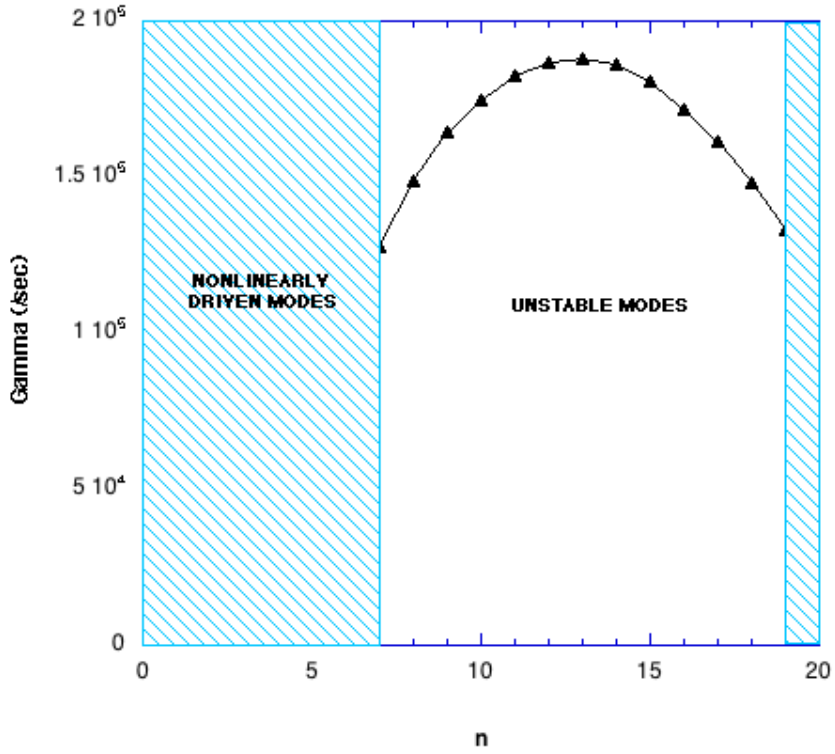

Figure 7. Linear growth rates measured from the early phase of the nonlinear simulation shows a broad spectrum peaked at n=13. The equilibrium is the same as the T_{ped}=700 eV profile of Figure 3.

The character of the non-linear behavior of the edge modes in this discharge is summarized in Figures 8-10, which show several properties of the discharge at selected times during the evolution. The upper right hand section of each of these figures shows color contours of the pressure in the $\phi = 0$ toroidal plane. The blue region represents the cold plasma outside the confinement region. The black overlaid contour is a surface at which the normal component of the convective heat flux ($q_V = \mathbf{n} \cdot \mathbf{V} nT$) is computed. (This simulation has a computational domain that extends "self-similarly" beyond the confinement region. The surface at which the heat flux is measured also conforms to the boundary, and the outboard midplane location corresponding to the position of the DIII-D wall.) The lower right hand section contains a Poincaré plot of the magnetic field-line punctures in the $\phi = 0$ toroidal plane. The lower left hand section shows perspective views of pressure contours at four toroidal planes equally spaced around the torus. This displays the three-dimensional structure of the dynamics. The upper left hand section shows color contours of the convective heat flux at the surface indicated by the black contour shown in the upper right hand section. This contour has been "unwrapped" into the poloidal-toroidal plane. Arrows show the relationships between the poloidal locations in this plot and the black contour in the figure to the right. Only the convective heat flux is shown because its contribution to the heat loss is greater than that of the conductive heat loss, in contrast to NIMROD simulation results on plasma disruption due to an internal mode [8].

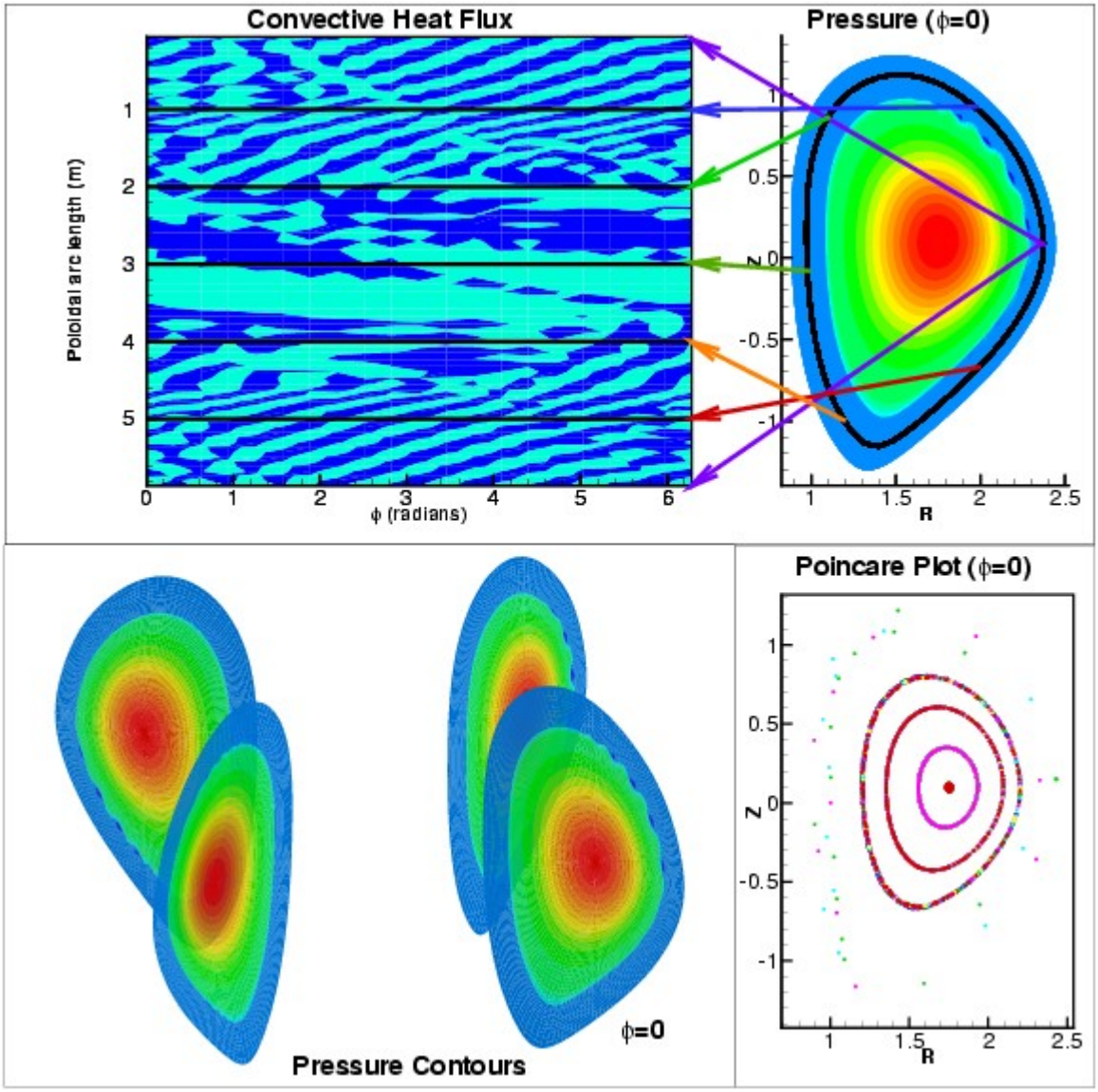

Figure 8. Convective heat flux as a function of poloidal arc length and toroidal angle is shown, at t=0.115 ms. Arrows indicate location of the measures of poloidal arc length. The three dimensional structure can be seen by the pressure contours in the lower left corner.

Figure 8 shows that configuration at t = 0.115 ms, the start of the nonlinear phase. Small corrugations are visible in the pressure contours, but the magnetic field-lines trace out nested flux surfaces, and there is no significant loss of heat. Figure 9 shows the configuration at t=0.144 ms, the time of peak amplitude of convective heat flux. Ribbons of plasma pressure now extend beyond the black boundary contour and have eroded a significant portion of the plasma core. The field in the edge has become stochastic, contributing to heat loss. The convective heat flux appears as bright spots on the boundary surface, primarily near the top and bottom of the chamber. An overall striation pattern in the heat flux deposition is evident. The striation pattern differs in the four major regions: outboard, top, bottom (separatrix), and inboard. The maximum heat flux is localized in the top and bottom regions with greatest concentration in the top region, where the triangularity of the equilibrium is not as strong. Figure 10 shows conditions at the end of the calculation, when the ribbons are retreating back toward the plasma. The mode structure increases in poloidal extent, and the heat flux structure shows little

difference between the top region and the upper inboard region. The differences between the upper inboard region and lower inboard region are due to the lower single null configuration of this plasma. These preliminary results suggest that high triangularity would be effective in preventing heat flux from reaching the inboard side. The magnetic field remains stochastic over much of the outer portion of the discharge.

The evolution is more dynamic than what is evident from still figures. An animation of the evolution represented by Figures 8-10 can be found at http://fusion.txcorp.com/~kruger/elma10n_images/elma10n.gif.

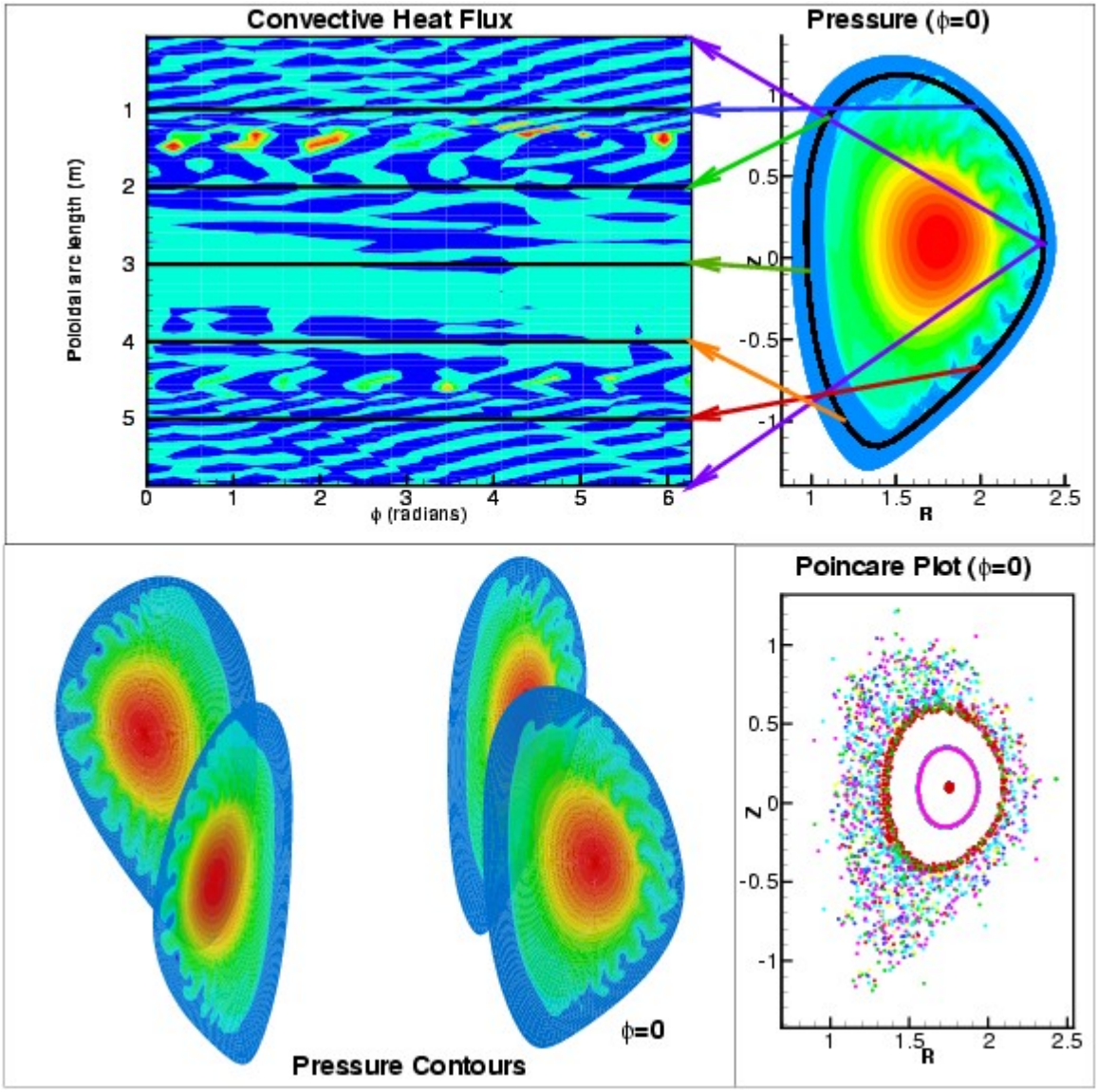

Figure 9. At t=0.144 ms, the heat load on the wall is at its peak. The three-dimensional load structure shows complicated structure that has penetrated toward the interior of the plasma.

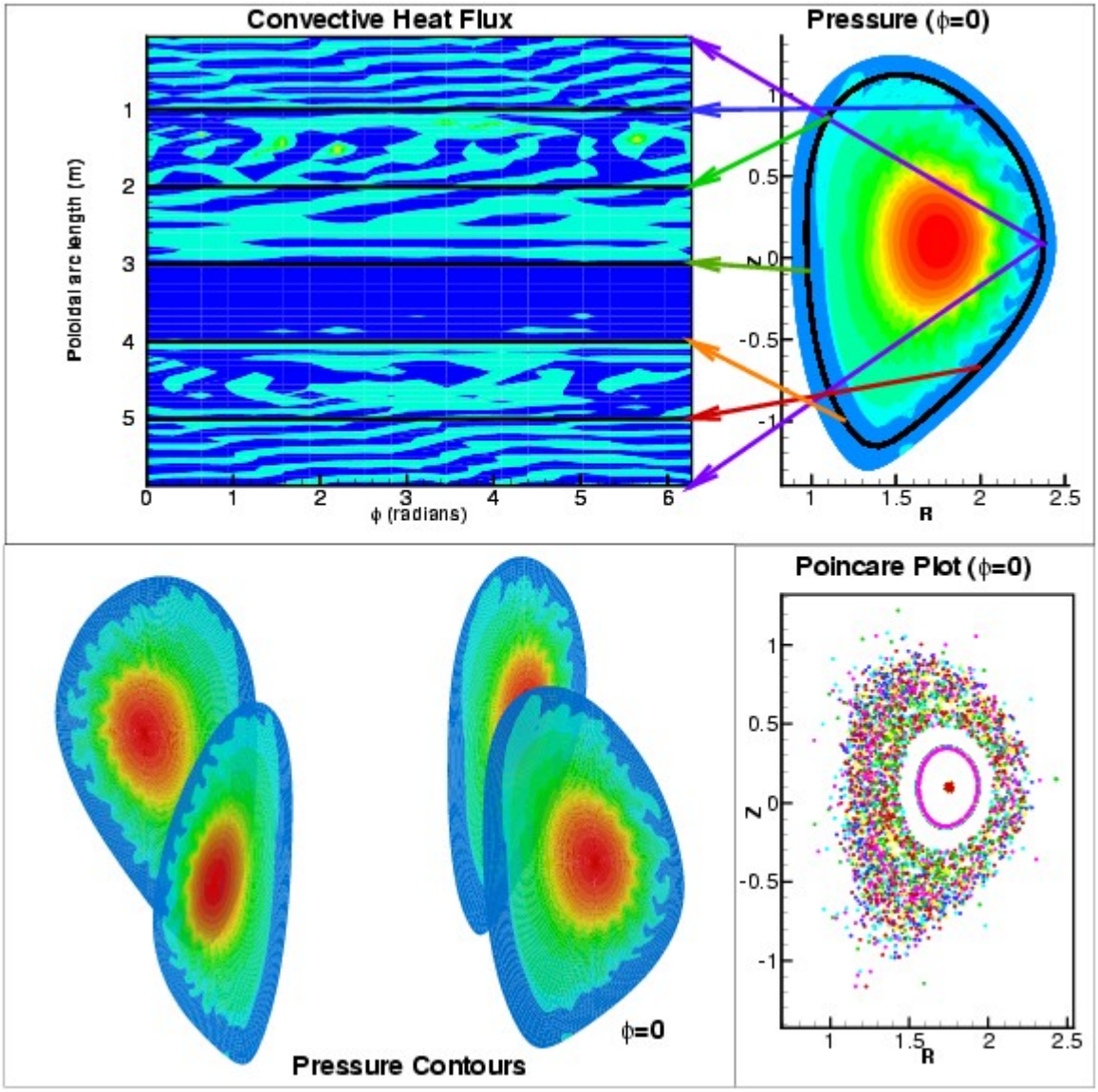

Figure 10. Near the end of the simulation, the poloidal extent of the mode has increased and the field is almost completely stochastic. The *n*=1 structure can be seen within the high harmonic structure.

The nonlinear evolution of this mode drives a rapid loss of internal energy with approximately 70 kJ (~10%) of the internal energy being lost within 60 μs, as shown in Figure 11. Laboratory measurements indicate 15-20% energy loss during large ELM events in DIII-D [1], and we note that the numerical simulation has not completed the ELM cycle. The internal energy is still decreasing at the end of the simulation while pressure is lost over the entire pedestal region. The computation finds that the primary loss channel is convective (n**T**$\mathbf{V}$) rather than conductive (**q**), which is not inconsistent with laboratory measurements [1].

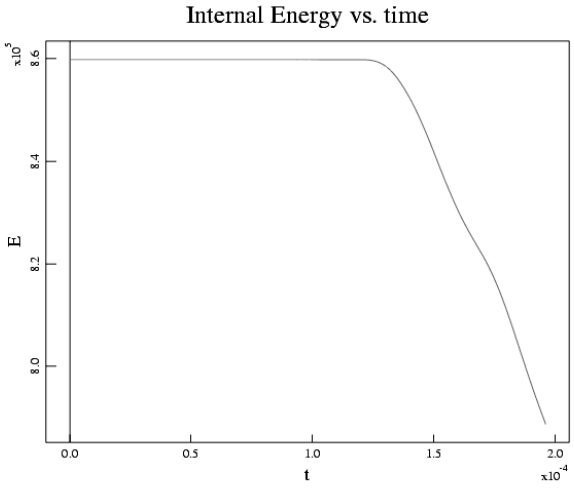

Figure 11. As a result of the nonlinear evolution of the ELM activity, approximately 10% of the internal energy is lost within 60 μs.

4.0. Discussion and Summary

Because of the deleterious effects of ELMs on plasma performance and operation, it is important to understand both their onset and the manner in which they deposit heat on the wall. A better understanding of onset will lead to operations and control techniques that avoid the most harmful form of ELMs. Knowledge of heat transport can be used to engineer configurations that are robust to ELM activity.

The linear studies in this report represent the first significant parameter scan to consider the effects of a separatrix and collisionality on ELMs. At present, the results must be considered preliminary, since more numerical convergence testing is needed. The results are sufficiently mature, however, to provide a useful guide for the requirements of nonlinear simulations. The nonlinear simulation presented here is the first to show significant plasma-wall interactions as a result of an ELM instability over a global computational domain. While the nonlinear simulation is also preliminary in many ways, it appears to reproduce some important experimental observations such as the energy loss time-scale and the heat loss mechanism. This suggests that nonlinear fluid simulations have potential to provide insight into how ELMs evolve and deposit heat onto the wall. Further refinements of the simulations will include more accurate geometry, improved boundary conditions, and more refined physics models, such as non-linear two-fluid and gyro-viscous effects.

References

[1] “Edge impurity dynamics during an edge-localized mode cycle on DIII-D,” M. R. Wade, K. H. Burrell, J. T. Hogan, A. W. Leonard, T. H. Osborne, P. B. Snyder, and D. Coster, Phys. Plasmas **12**, 056120 (2005).

[2] “Nonlinear magnetohydrodynamics simulation using high-order finite elements,” C.R. Sovinec, A.H. Glasser, D.C. Barnes, T.A. Gianakon, R.A. Nebel, S.E. Kruger, D.D. Schnack, S.J. Plimpton, A. Tarditi, M.S. Chu and the NIMROD Team, J. Comput. Phys. **195**, 355 (2004).

[3] “Edge localized modes and the pedestal: A model based on coupled peeling--ballooning modes,” P. B. Snyder, H. R. Wilson, J. R. Ferron, L. L. Lao, A. W. Leonard, T. H. Osborne, A. D. Turnbull, D. Mossessian, M. Murakami, and X. Q. Xu, Phys. Plasmas **9**, 2037 (2002)

[4] “Numerical studies of edge localized instabilities in tokamaks,” H. R. Wilson, P. B. Snyder, G. T. A. Huysmans, and R. L. Miller, Phys. Plasmas **9**, 1277 (2002)

[5] “Progress in the peeling-ballooning model of edge localized modes: Numerical studies of nonlinear dynamics,” P. B. Snyder, H. R. Wilson, and X. Q. Xu, Phys. Plasmas **12**, 056115 (2005)

[6] C. R. Sovinec, D. D. Schnack, A. Y. Pankin, D P. Brennan, H. Tian, D. C Barnes, S. E. Kruger, E. D. Held, C. C. Kim, X. S Li, D. K. Kaushik, S. C. Jardin and the NIMROD Team, “Nonlinear extended magnetohydrodynamics simulation using high-order finite elements,” Journal of Physics: Conference Series **16**, 2005.

[7] E. D. Held, J. D. Callen, C. C. Hegna, C. R. Sovinec, T. A. Gianakon, and S. E. Kruger, “Nonlocal closures for plasma fluid simulations,” Phys. Plasmas **11**, 2419 (2004).

[8] “Dynamics of the major disruption of a DIII-D plasma,” S. E. Kruger, D. D. Schnack, and C. R. Sovinec, Phys. Plasmas **12**, 056113 (2005)

Quarterly Fusion Theory Milestone Report for 2006 Quarter 1 12/31/05

S.E. Kruger and D.D. Schnack

I. Executive Summary

In this report, we present the successful completion of the 2006 Q1 milestone, namely: an n=0 steady-state near the 2005 700 eV equilibria was found. Because the H-mode equilbria used in the ELM studies are the most challenging equilibria ever used by nonlinear initial-value, extended MHD codes, details on the numerical challenges are presented. This quarterly milestone motivated new development of the NIMROD code: namely more flexibility in source specification and run time operation. These development will allow NIMROD more flexibility in meeting the challenges of subsequent milestones.

II. Statement of Problem

At the conclusion of the 2005 ELM milestone, the NIMROD code successfully ran an ELM simulation far into the nonlinear regime allowing for the study of heat flux on the wall. Even in those successful simulations, numerical difficulties occurring at the separatrix occurred well beyond where a "separatrix" could be clearly defined. Because of NIMROD's "separation of equilibrium variables" (to be discussed in Section III.B.), these problems were believed to be associated with how the $n = 0$ steady-state fields are initialized. The M3D code observed similar numerical problems when using the equilibrium as given. Because of these problems, the first quarterly milestone was chosen to investigate the $n = 0$ solutions and determine a more appropriate initialization – one that would prevent numerical issues. The ability to have an appropriate $n = 0$ state as the initial condition will prepare the codes for the more challenging milestones in the coming year.

III. Technical Background

A. Equilibrium Definition

In tokamaks, the plasmas are often quiescent with very little non-symmetric components of the fields. It is the low-frequency, long-wavelength deviations away from this symmetry that is studied with nonlinear, initial-value, extend MHD codes. To study the deviations, extended MHD simulations of large tokamaks generally start with symmetric fields coming from a Grad-Shafranov equilibrium. As discussed below, the Grad-Shafranov equilibrium is a subset of the steady-state MHD equations. Considerable effort has gone into experimentally reconstructing the symmetric fields based on the Grad-Shafranov model. The most widely-used code for performing this reconstruction is the EFIT code from General Atomics. Because we are interested in nonlinear simulations of ELMs, the equilibrium code used to initialize the code must include the separatrix; i.e., it must be a *free-boundary GS solver*. Beyond EFIT, a widely-used code for this purpose is the TEQ code from LLNL.

To place the initial conditions of the nonlinear initial-value codes in context, we briefly review the extended MHD equations. The extended MHD equations that we are solving are:

Continuity: $$\frac{\partial \nu}{\partial \tau} + \nabla \cdot \varsigma = 0 \quad , \qquad (1a)$$

Momentum: $$Mn\frac{d\mathbf{V}}{dt} = -\nabla p + \mathbf{J}\times\mathbf{B} - \nabla\cdot\Pi_{visc} - \nabla\cdot\Pi_{gv} - \nabla\cdot\Pi_{\parallel} \quad , \quad (1b)$$

Gen. Ohm's Law: $$\mathbf{E} = -\mathbf{V}\times\mathbf{B} + \frac{1}{ne}[\mathbf{J}\times\mathbf{B} - \nabla p_e - \nabla\cdot\Pi_e] + \eta\mathbf{J} \quad . \quad (1c)$$

Energy: $$n_\alpha\left(\frac{\partial T_\alpha}{\partial t} + \mathbf{V}_\alpha \bullet \nabla T_\alpha\right) = (\gamma - 1)[\nabla \bullet \mathbf{q}_\alpha + ...]. \quad (1d)$$

where ***J*** is the plasma current density, and *p* is the plasma pressure (total unless subscripted for the species). To form the complete set of evolution equations, we use the "pre-Maxwell equations"; i.e., Maxwell's equations without the displacement current.

Div(B): $$\nabla\cdot\mathbf{B} = 0 \quad , \quad (2a)$$

Ampere's Law: $$\nabla\times\mathbf{B} = \mu_0\mathbf{J} \quad , \quad (2b)$$

Faraday's Law $$\frac{\partial\mathbf{B}}{\partial t} = \nabla\times\mathbf{E} \quad , \quad (2c)$$

The lack of displacement current (and concomitant disregard of Gauss's Law) is the "quasineutrality" approximation, which is $|q_e|n_e = q_i n_i$. This approximation is valid for the low frequencies ($\omega^2 << c^2k^2$) studied in extended MHD.

The form of the generalized Ohm's law (Eq. 1.c) generally distinguishes the commonly used extended MHD. In this document, we will make reference to three models: ideal MHD, resistive MHD, and extended MHD. These are:

Ideal MHD: $$\mathbf{E} = -\mathbf{V}\times\mathbf{B} \quad (3a)$$

Resistive MHD: $$\mathbf{E} = -\varsigma\times\mathbf{B} + \eta\vartheta \quad . \quad (3b)$$

Extended MHD: $$\mathbf{E} = -\mathbf{V}\times\mathbf{B} + \frac{1}{ne}[\mathbf{J}\times\mathbf{B} - \nabla p_e - \nabla\cdot\Pi_e] + \eta\mathbf{J} \quad . \quad (3c)$$

In addition to neglecting the resistivity, ideal MHD ignores all other dissipative terms (i.e., no viscosity and all terms on right-side of Eq. 1.d. are neglected). Resistive MHD traditionally has neglected all terms on right-side of Eq. 1.d. although there is no standard nomenclature in the literature.

To derive the "steady-state" solutions of the extended MHD equations, two assumptions are usually made: (1) the diffusive terms operate on time-scales much longer than the "steady-state" and can be neglected, and (2) we consider $n = 0$. The first assumption allows the definition of "steady-state" to be the transport time scale, which is generally much slower than the time scales of the instabilities we wish to study. This is discussed further in Section III.B. Using these assumptions, the relevant equations are:

Continuity: $$\nabla\cdot n_0\mathbf{V}_0 = 0 \quad , \quad (4a)$$

Momentum: $$mn_0\mathbf{V}_0 \bullet \nabla_0\mathbf{V}_0 = -\nabla p_0 + \mathbf{J}_0\times\mathbf{B}_0 \quad , (4b)$$

Gen. Ohm's Law: $$\mathbf{E}_0 + \mathbf{V}_0\times\mathbf{B}_0 = \frac{1}{n_0 e}[\mathbf{J}_0\times\mathbf{B}_0 - \nabla p_{e0} - \nabla\cdot\Pi_{e0}] \quad . \quad (4c)$$

Energy: $$n_{\alpha 0}(\mathbf{V}_{\alpha 0} \bullet \nabla T_{\alpha 0}) + \gamma n_{\alpha 0} T_{\alpha 0}\nabla \bullet \mathbf{V}_{\alpha 0} = 0 \quad (4d)$$

In addition to the two assumptions above, two other assumptions are commonly made: 1) No equilibrium flow, and 2) Neglect the two-fluid terms (right side of Eq. 4c); i.e., only consider ideal MHD.

The first assumption allows the momentum equation (Eq. 4b) to decouple from all other equations. The momentum equation can then be written in a form called the Grad-Shafranov Equation. All linear MHD codes use this as their input. Note that in this case, the Ohm's law can be solved independently of the Grad-Shafranov equation to determine the current sources. Separate codes are usually used to determine what fraction of the current comes from Ohmic drive, bootstrap current (from the stress tensor term in Eq. 4c), Pfirsch-Schluter currents, and current drive.

Removing the first assumption, but keeping the second, allows the derivation of a modified Grad-Shafranov equation [Hameiri81]. For purely toroidal flow, the modifications are rather trivial and implemented by several codes. While more accurate, these modifications are generally not included in equilibrium reconstructions because the characteristic flows in experiment are generally a quarter of the Mach speed, which gives corrections that are small compared to other uncertainties in the equilibrium reconstruction. It is hoped that as diagnostic improve, especially in determining the flow profiles, the inclusion of this term will become more routine. For flows that are both poloidal and toroidal, the modified Grad-Shafranov equation includes a singularity when the polodial flow reaches the poloidal Alfven Mach number. Because of poloidal flow damping, poloidal flows are generally unimportant, although they may be significant near the edge. With the exception of a recent code written by a student of Betti, [need ref], no code includes poloidal flow.

Removing all assumptions regarding equilibrium solutions has been done only recently. Inclusion of the two-fluid terms automatically requires the inclusion of the inertia term in the momentum equation to have the proper treatment of the drift flows. No code currently solves for the two-fluid equilibrium equations, nor are any initial value codes prepared to accept two-fluid equilibria. In the future, including this capability may be important for the extended MHD codes.

B. Separation of Variables and Diffusive Sources

For the technical discussion below, we will discuss two separate modes of operation for the NIMROD code: "separated equilibrium mode" and "$n = 0$ mode". The general prescription for deriving the form of the equations solved in NIMROD is to separate the quantities into a "steady-state component" and a dynamic component: $Q(\mathbf{r},t) = Q_{ss}(\mathbf{r}) + \tilde{Q}(\mathbf{r},t)$. In all subsequent equations, the terms that contain purely steady-state factors are not explicitly included; rather, they are assumed to satisfy the constraints given by Eq. 4 and hence do not appear in the dynamical equations. *The dynamical component thus represents the deviation from the steady state solution given in Eq. 4*; it does *not* represent the total plasma state. This has implications on the interpretation of the equations. To understand this, we consider this prescription for a purely diffusive pressure equation:

$$\frac{\partial p}{\partial t} = \chi \nabla^2 p \qquad (5)$$

where we assume a constant diffusivity. With homogeneous Dirichlet boundary conditions, the steady-state solution of this is *p=0*. Separating into dynamic and stready state solutions, the dynamic equation is:

$$\frac{\partial \tilde{p}}{\partial t} = \chi \nabla^2 \tilde{p} \quad (6)$$

The steady state solution is $\tilde{p} = 0$. The total pressure is $p = p_{ss} + \tilde{p} = p_{ss}$. *Note that here* $\pi_{\sigma c}$ *is assumed to exist and be maintained by some external mechanism*. The implication is that a source has implicitly been added to the equation. This has been the default manner in which NIMROD has run – in particular, the successful ELM milestone was performed using this method.

To understand the implications better, we want to rewrite our equation with an explicit source:

$$\frac{\partial p}{\partial t} = \chi \nabla^2 p + S_p \qquad (7)$$

To derive Eq. (7), the cancellation is $S_p = -\chi \nabla^2 p_{ss}$; that is,

$$\frac{\partial p}{\partial t} = \chi \nabla^2 p - \chi \nabla^2 p_{ss} \quad (8)$$

so that $\partial \pi / \partial \tau = 0$ when $\pi = \pi_{\sigma c}$. We term this type of source a "diffusive source" and it is can be present in all of the equations that have a diffusive term. The physical effect of the source is to maintain the equilibrium profiles. (This assumes the diffusivity is fixed. Temperature-dependent diffusivities will have slightly different behavior). The advantage of using the sources is that for tokamak runs they approximate the real sources within a tokamak for the time-scales under consideration.

The point is that Eq. (6) (for the "dynamical" component) and Eq. (8) (for the "total" component) are mathematically equivalent. The default way for NIMROD to run tokamak simulations has been to use Eq. (6). We can solve Equation (5), which is the equivalent of Eq. (8) (informally called the "transfer eq mode" on the NIMROD team) without the sources. The M3D team uses the equivalent of Eq. (8).

IV. Technical Approach

A. Characterization of the Equilibrium

In this work, we only investigate the "Pedestal T_e=700 eV" equilibrium because it was the case used in the 2005 Milestone case. The results and implications of this study are generic to H-mode equilibria in general.

The equilibrium is shown in Fig. 1. As shown, the current density is localized near the separatrix. Although the equilibrium was constructed such that the flux surface average of parallel gradient ($\langle J.B/B^2 \rangle$) is zero, there are large local poloidal variations in the poloidal current. The toroidal gradient is defined to be exactly zero beyond the separatrix. Although the experiment has some finite current in the scrape-off-layer (SOL) region, at this time there is no satisfactory method to obtain those currents in such a way that the equilibrium conditions are exactly satisfied.

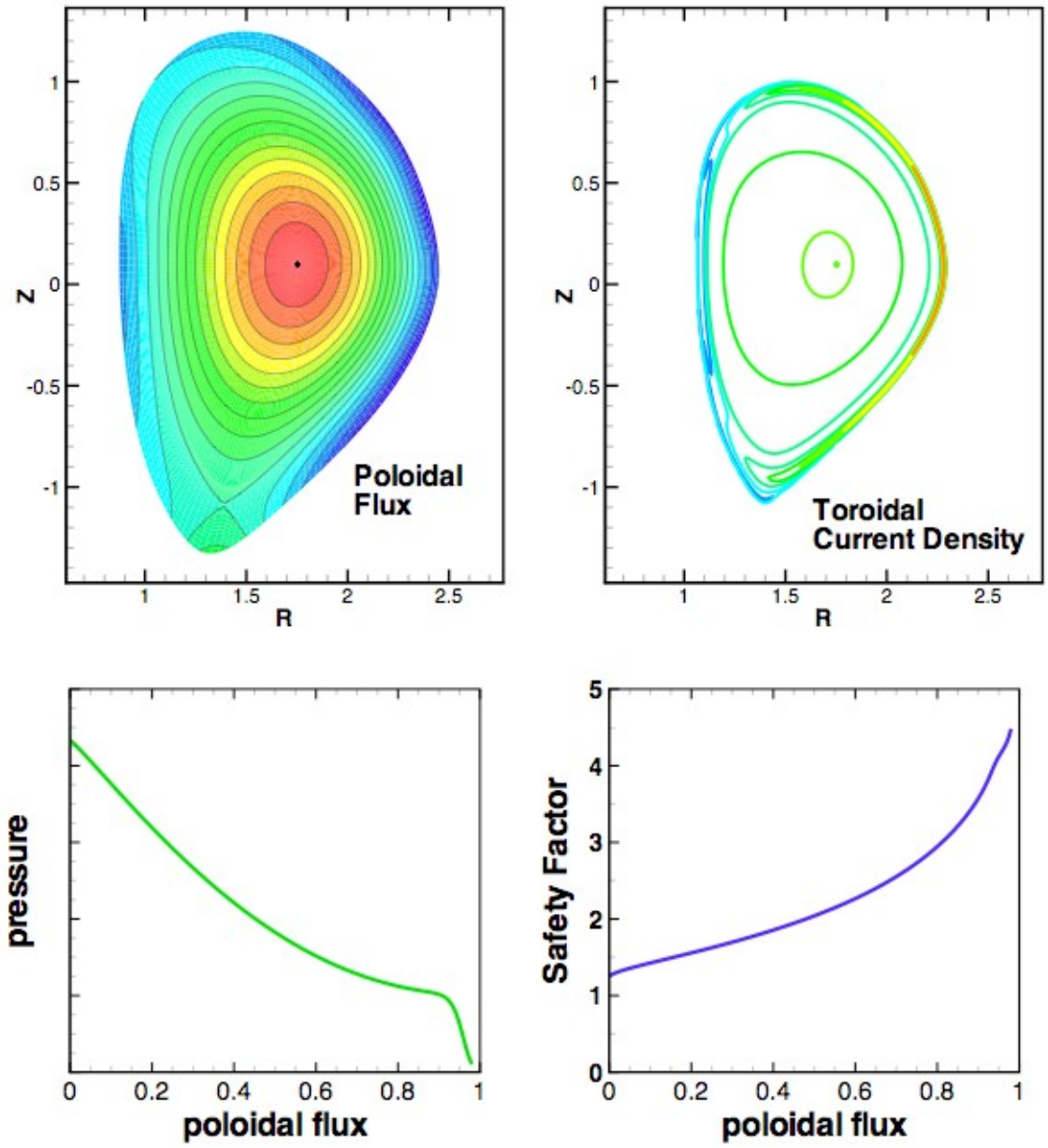

Figure 6. The equilibrium used in the 2005 Milestone report has a large localized toroidal current gradient near the separatrix, and a strong poloidal variation in the current, despite the fact that the flux surface average of the parallel current is constant.

The effect of the sharp current gradient can be seen in the cylindrical components of the poloidal magnetic field shown in Figure 2. The sharp discontinuities at the separatrix are readily apparent. Also apparent are the rapid variations of magnetic field on the inboard

side. This is caused by the existence of the poloidal magnetic field coils on the inboard side. The equilibrium codes numerically handle the coil fields using a Greene's function technique which allows them to avoid the difficulties of the fields near the coils.

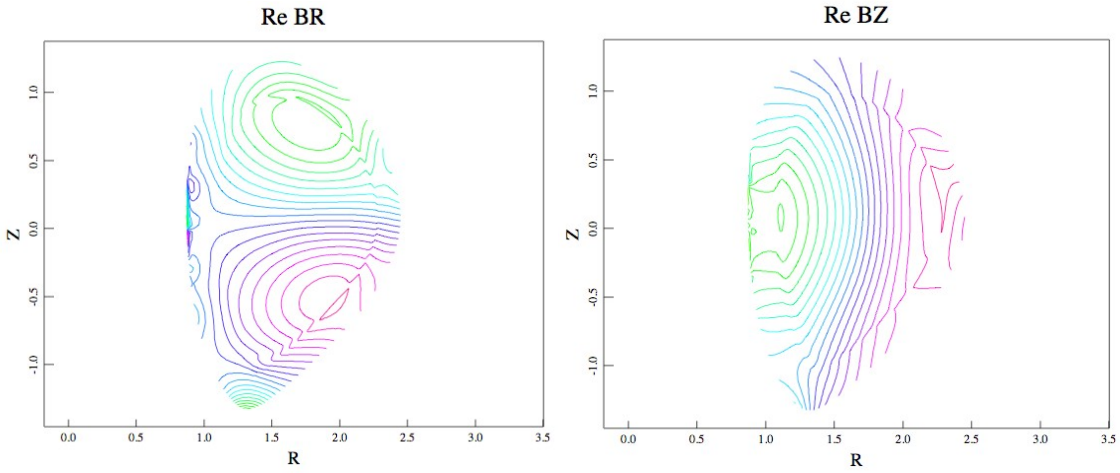

Figure 7. The cylindrical components of the magnetic field show the sharp discontinuities due to the sharp current gradients as well as the effect of poloidal field coils on the inboard side of the plasma.

As discussed in Section II.B., the 2005 Milestone simulations were run with "implicit sources". i.e., the form given by Eq. 6. Because we had no equilibrium flow, there were no momentum sources. Because we evolved only the total temperature, there was no electron pressure source. The sources were thus are a current source and a pressure source. As the equilibrium parameter plots of Figure 1 suggests, these implicit sources are highly localized. In addition to the large, localized gradients, the temperatures are low leading to large diffusivity parameters (when using Braginskii coefficients). In Figure 3, the source for the resistive Ohm's law and temperature equation are shown when Braginskii coefficients are used (for the 2005 Milestone case, the Braginskii resistivity was used for the resistive Ohm's law.). Clearly these fixed sources play an important role in the ensuing dynamics

The NIMROD runs to date have used these sources in the "separated equilibrium mode" ($Q(\mathbf{r},t) = Q_{ss}(\mathbf{r}) + \tilde{Q}(\mathbf{r},t)$) and have generally been successful. The simulations are difficult, and in this work we will investigate the extent to which the sources can cause problems. The M3D code has performed their initial simulations by reaching a nearby steady-state using the code itself, i.e, solving Eq. 8. Our goal is to reach a similar state.

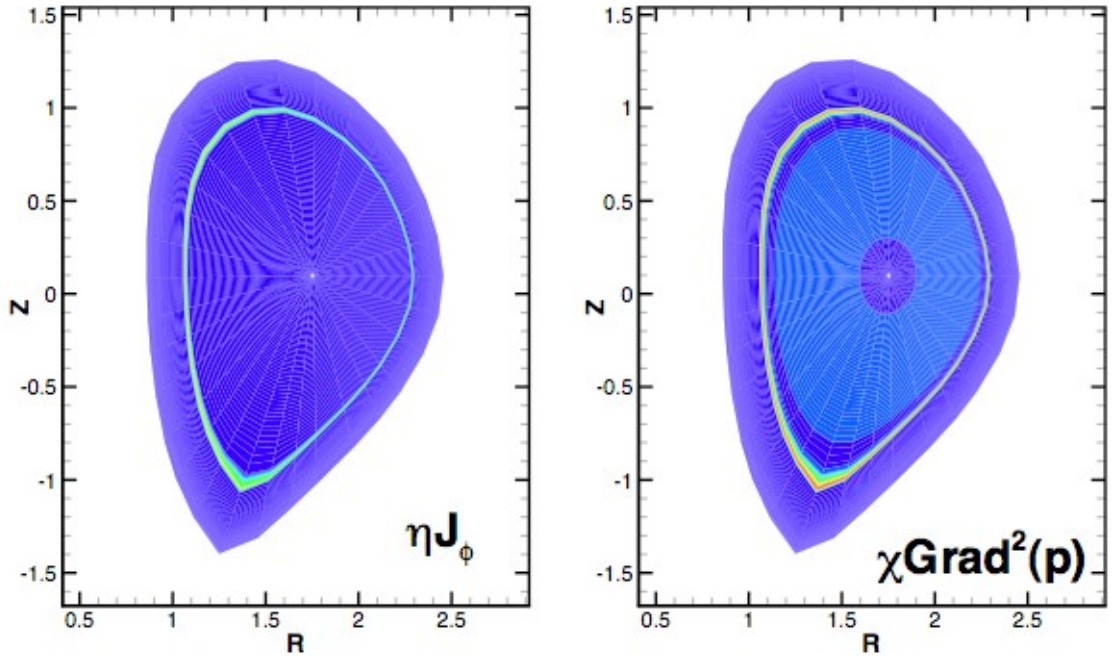

Figure 8. The diffusive sources in H-mode equilibria are very large near the separatrix when using Spitzer values. The low temperatures lead to large diffusivity values and H-mode equilibria have sharp edge pressure and current gradients.

B. Comparison of NIMROD modes of operation at low diffusivity

We are ready to discuss the $n = 0$ behavior of the ELM equilibria. We wish to study investigate the $n = 0$ behavior of the 2005 Milestone case with parameters similar to the results presented in the final report. The case has 36x40 cells with polynomial degree of 3. The temperature-dependent resistivity is evolved with a realistic $S = 1\text{x}10^8$. The peak resistivity is constrained to be 243 times the lowest resistivity. The viscosity is constant throughout the domain with a Prandtl number in the core of 6,250, and a Prandtl number in the vacuum region of 26. The viscous diffusivity and perpendicular thermal diffusivity are 25 m^2/s, and the parallel thermal diffusivity is 10^5 times larger.

We present two types of simulations: a "separated equilibrium" simulation that has implicit diffusive sources (i.e., Eq. (6)), and a "transferred equilibrium" simulation that has no source to maintain the fields (i.e., Eq. (5); in this case the "steady state" component of the solution appears only as an initial condition) . The time histories of the kinetic energy of the two runs are shown in Figure 4. As shown, after one microsecond, the energies differ by more than 13 orders of magnitude. Since we do not believe the $n = 0$ mode is inherently unstable, we conclude that *the initial "steady state" solution, as given by the Grad-Shafranov reconstruction from the experimental data, is not in sufficient force balance.*

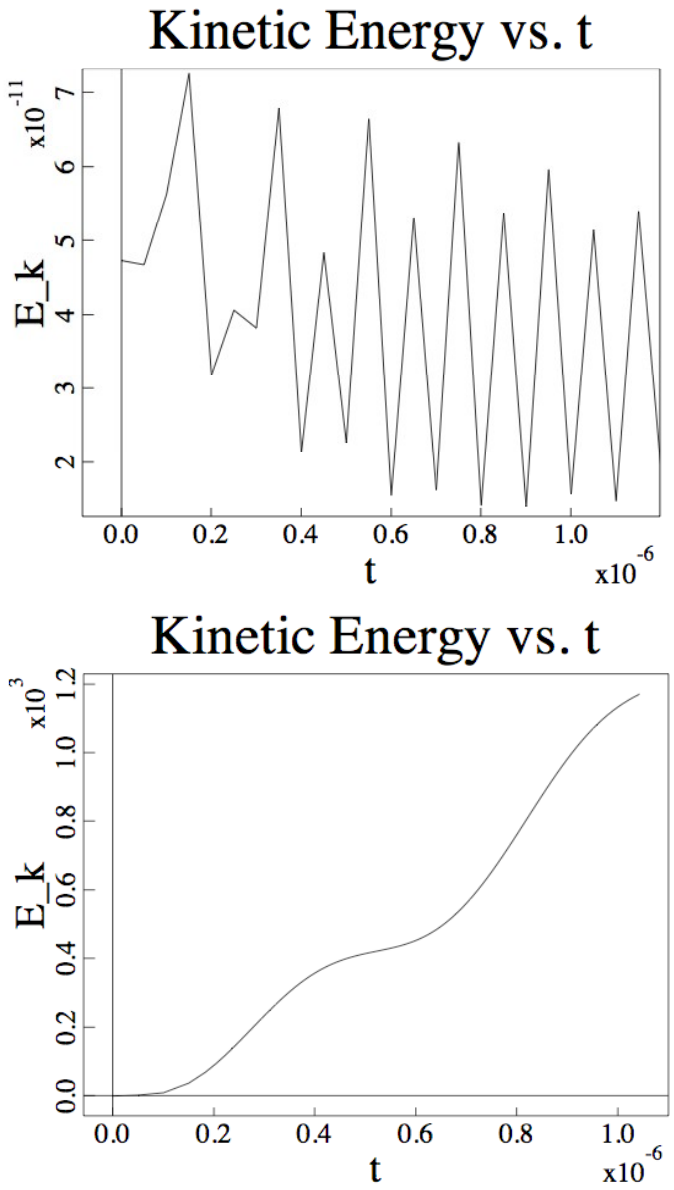

Figure 9. A comparison of two modes of NIMROD operation show a dramatic difference in behavior. The top assumes that the steady state is in exact force balance. The bottom uses the steady state as initial conditions. In one microsecond, the resultant kinetic energies differ by 13 orders of magnitude.

To explore the cause of the difficulties in the transferred equilibrium simulation (with the steady state used as initial conditions), we examine the behavior early in the time history. In Figure 5, we show plots of the radial (using major radius of the tokamak) of the velocity (because it is the largest component), and the toroidal current density (not the contravariant component). After the first time step, the current density has significant inboard current fluctuations. The reason for this is that the "equilibrium current" in this case is computed from using Faraday's law (Equation 2(b)) using the finite-element representation of the magnetic field shown in Figure 2. Because of the transfer of fields from one discretization scheme (in this case finite difference and spectral Greene's functions) to another (a finite-element mesh), the errors manifest themselves as large toroidal current fluctuations. These toroidal current fluctuations then act to drive large

flows. This is because the reconstructed solution is not in steady state on a sufficiently long time scale when transport effects are taken into account.

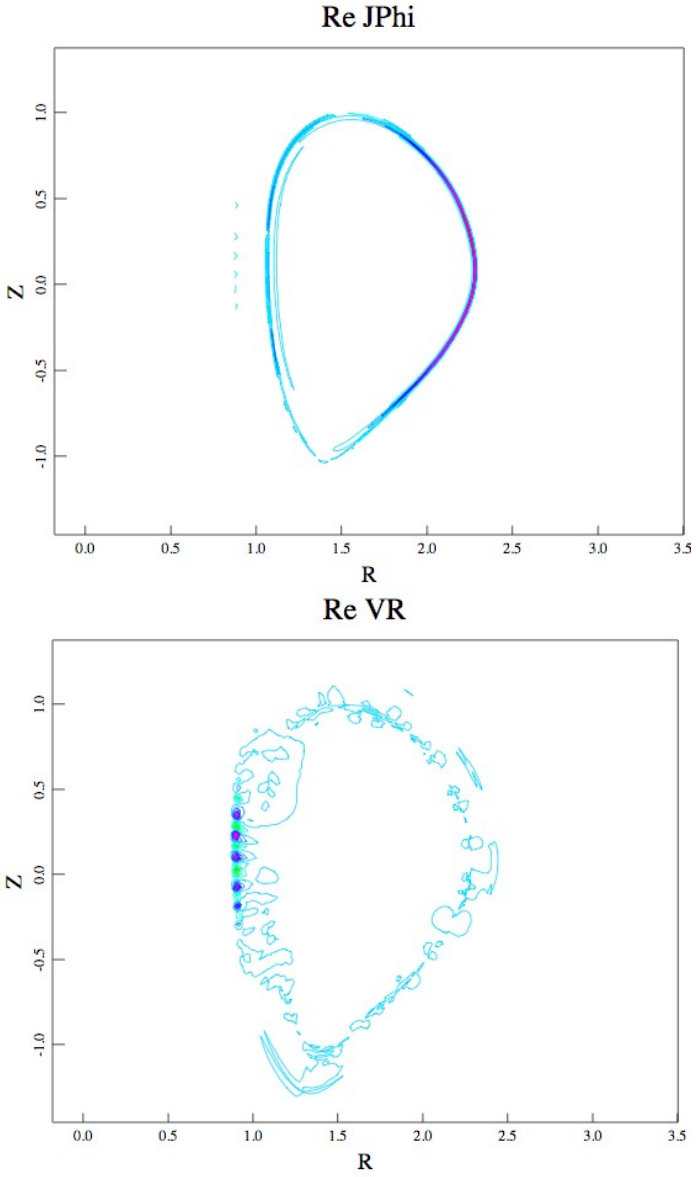

Figure 10. On the first time step, the toroidal component of the current density shows significant fluctuations on the inboard side near the poloidal flux coils. These fluctuations drive large flows on the inboard side within the first time step.

The same quantities are shown in Figure 6 after 90 time steps later (t_{sim}=9.4 x 10^{-7} sec). At this time, one can see that the induced numerical noise is beginning to broaden, and is not dominant at the edge. From both Figures 5 and 6 we note the separatrix location is clearly identified. Two sources of difficulties can be seen in these initial studies: 1) the equilibrium fields on the inboard midplane are difficult to numerically simulate because the rapidly varying magnetic fields there, and 2) the separatrix presents its own source of difficulties.

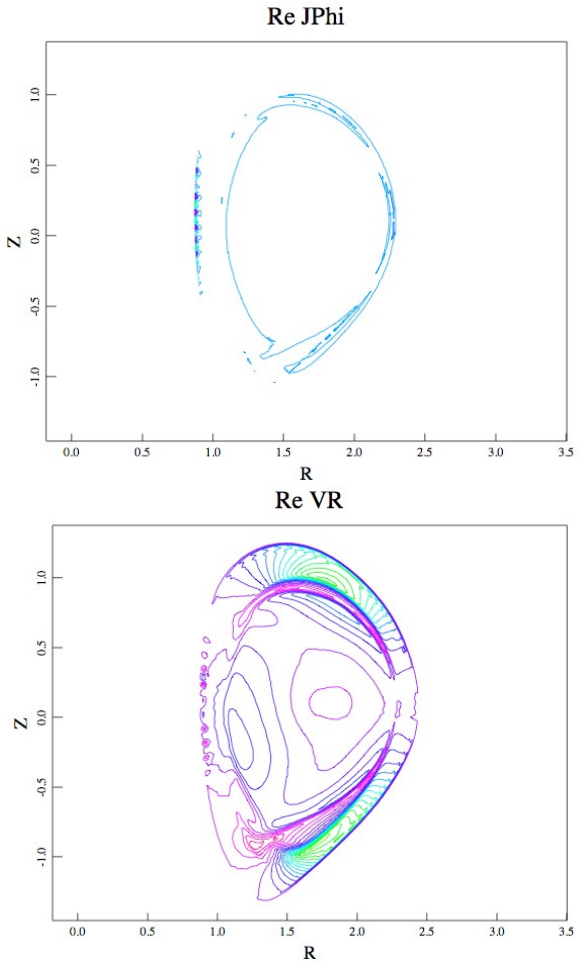

Figure 11. The velocity field begins to broaden although the difficulties with the current density still remain.

C. Development of an $n = 0$ steady-state solution

The typical method for developing an $n = 0$ steady-state solution for subsequent initialization is to add large diffusivities to the equations and just evolve the $n = 0$ solution to a time assymnptotoc steady state (referred to as "equilibrium relaxation"). This method is used by the M3D code, the TSC transport code, and the HINT code for three-dimensional equilibria. The advantage of this approach is that it is a robust method for finding suitable equilibria for subsequent simulation. The disadvantage is that it can complicate the analysis of the simulations when the parameters depend sensitively on the equilibria used. (The equilibria obtained from "relaxation" may differ in local detail from the original Grad-Shafranov equilibrium.)

The NIMROD code has not extensively performed simulations of this type (i.e., "relaxation") for tokamak equilibria. The goal of this work is to not only perform these types of simulations, but take advantage of NIMROD's separated equilibrium functionality and investigate its role in the development of a steady-state solution; i.e., why do separated equilibria work so well? The discussion of Section III.B suggests that it is because the toroidal current, which is inconsistent with the magnetic field representation in the equilibrium reconstruction, is more accurate on the inboard midplane. However, the difficulties at the separatrix also point to the existence of problems there. Do the implicit diffusive sources help in these cases?

To answer these questions, the NIMROD code was programmed to add to new capabilities: running in the transferred equilibrium mode with diffusive source (i.e., Eq. (8)), and running with the separated equilibrium mode with no sources. This gives us 4 cases to compare: with and without separated equilibrium, and with and without sources. Because of the difficulties with the current discussed above, the simulations are run at S = 1.354E+03 in the core, to be able to have the transferred equilibrium cases run and allow accurate comparisons. The viscosities are run at values of 25, 250, 2500, and 25000 m^2/s. The thermal diffusivities are held to the same values as the cases discussed in Section III.B. Although anisotropic thermal conduction is generally considered unimportant, it was included in the simulations to ensure a proper equilibration of the n = 0 steady-state.

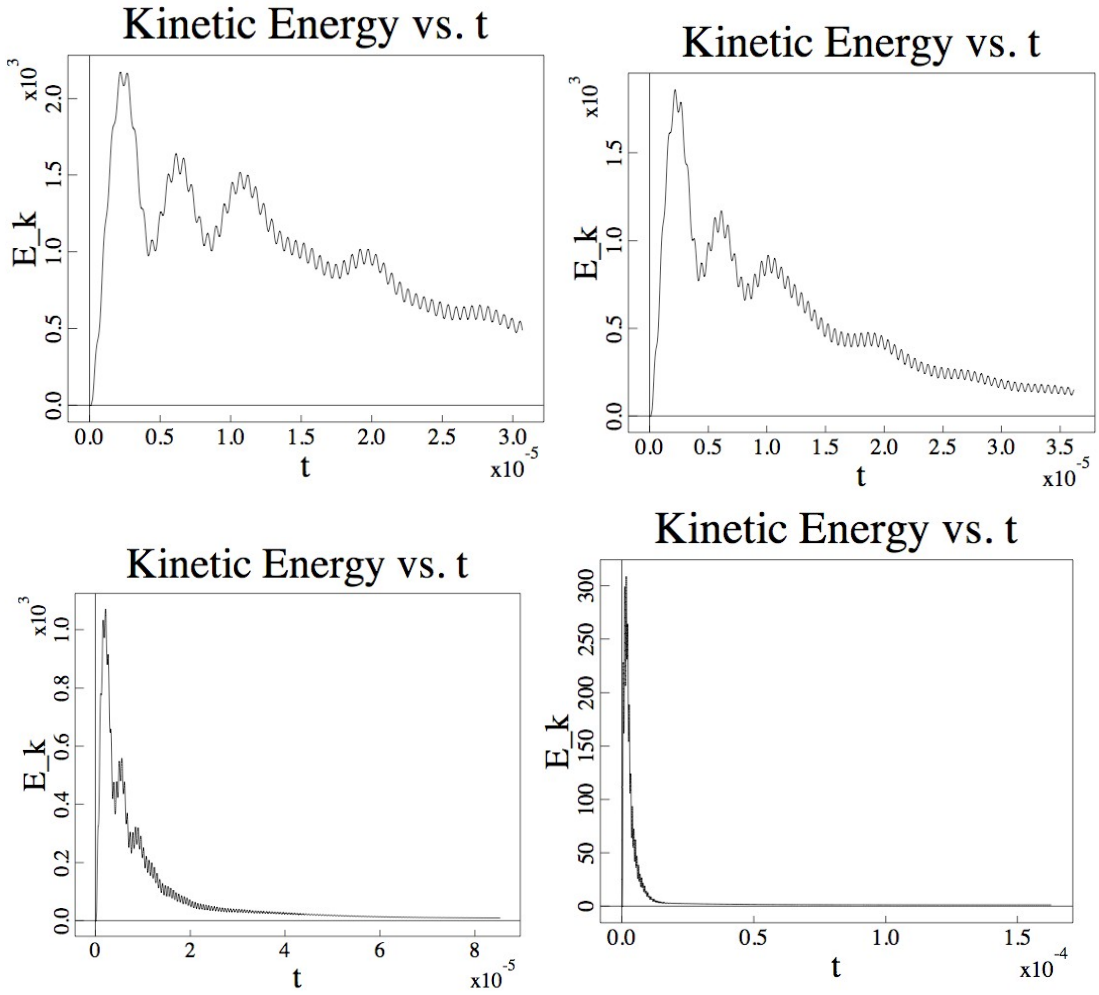

Figure 12. Time history plots for the transferred equilibrium case with sources for kinematic viscosities of 25, 250, 2500, and 25,000 m^2/s.

We first discuss the transferred equilibrium cases. The time history plots for the cases with and without sources are quantitatively similar. For simplicity, only the time history plots for the case with sources is shown. The peak kinetic energy and decay time corresponds to the magnitude of the viscosity as one would expect. The two highest cases have clearly reached an n = 0 steady-state as shown.

The types of steady state reached are different. Considering only the largest viscosity for simplicity, we compare the toroidal current and magnetic field in Figure 8. As expected, the case that has a source acting to maintain the equilibrium has a

steady-state that is closer to the original equilibrium. The case without sources has smoother fields.

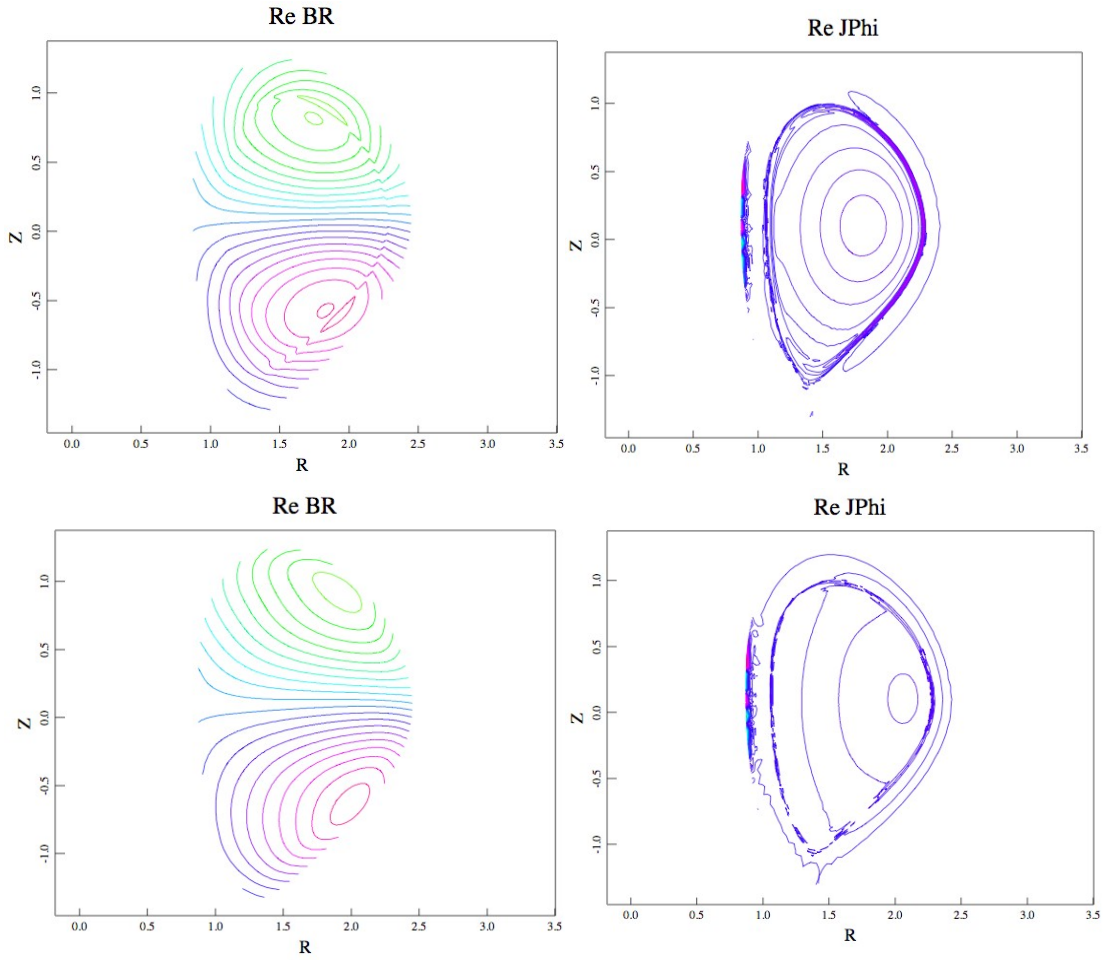

Figure 13. A comparison of the transferred equilibrium cases with sources (top) and without sources (bottom). The magnetic field for the case with sources looks similar to the magnetic field shown in Fig. 2 unlike the case without sources.

The separated equilibria cases have much different behavior. We first consider the typical NIMROD run which has the implicit diffusive sources. All of the cases with the various viscosities have a similar time history plots with the kinetic energy never rising above 10^{-10} Joules. With such small changes, there is essentially no discernible differences in the equilibria from what has been shown in Figures 1 and 2, so they will not be shown.

The case of separated equilibria with no sources shows some interesting differences from the equilibrium cases. As one would expect, the plasma evolves to move away from the having the sharp gradients, with the time scale corresponding to the viscosity time scale. The time history plots of the kinetic energy is shown for two viscosity cases in Figure 9. After relatively fast transients, the plasma evolves on a transport time scale as expected. For the highest viscosity case shown in Figure 10, the current density peak is slightly broader than previous cases as one would expect. The overall magnetic field differs a little from the equilibrium magnetic field, but not significantly.

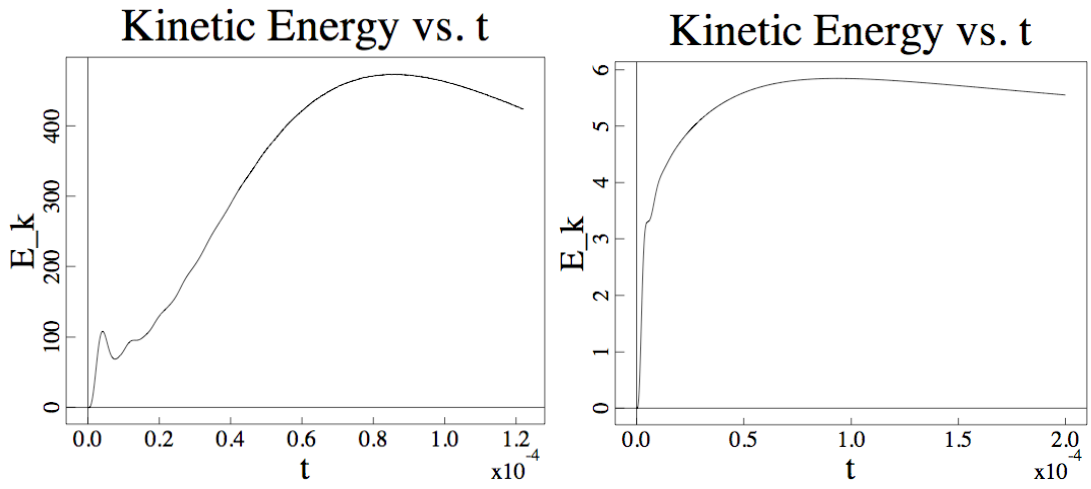

Figure 14. The time history plots of the kinetic energy for the separated equilibrium case with no sources for the viscosities of 250 (left) and 25,000 (right).

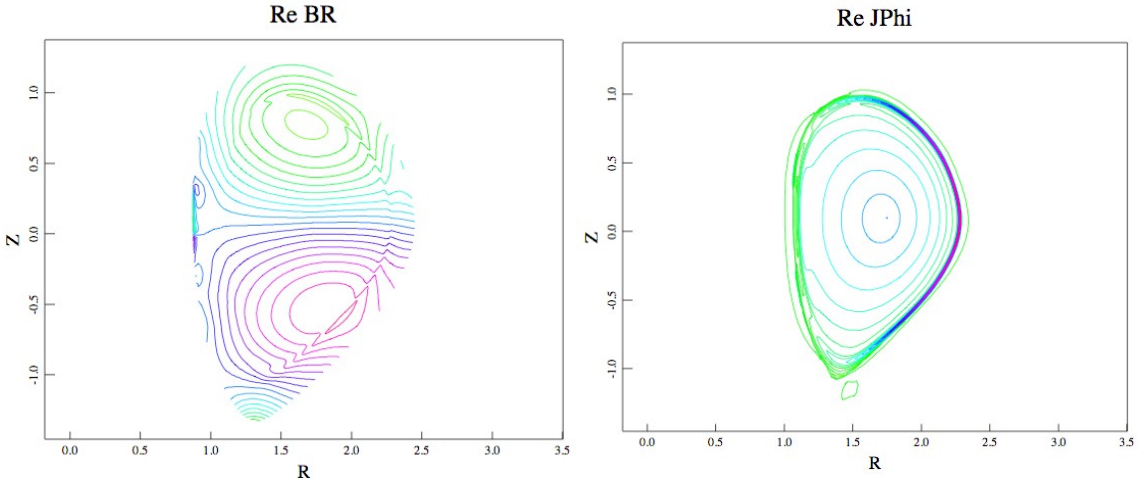

Figure 15. The torodial current density and magnetic field are very similar to the equilibria, but slightly broader. The current extends into the open field region slightly.

V. Conclusions

Nearby, $n = 0$ steady state solutions have been found using two different numerical methods under two different simulation conditions: with and without sources. The quality of the "separated equilibrium mode" greatly surpasses that of the "transferred equilibrium mode", and in the near term is likely to be the preferred method of running NIMROD. The development of the code to allow for each mode of operation to include or neglect the sources is beneficial to performing these types of studies and has greatly increased the flexibility of the code.

In this work, we have focused on creating an $n = 0$ steady-state that can be used to create a well-posed initial condition for the nonlinear simulations. The larger question is what is the right initial condition for studying the physics we want. To date, the equilibria have primarily been chosen based on its linear MHD stability properties. As we move forward, we will need more information from transport codes so that all of the profiles can simultaneously satisfy the steady-state condition. As shown above, understanding the sources is very important, and will only increase in importance as we move to two-fluid studies.

Although we state transport code information is needed, we note in passing that the ability to work with high-quality free-boundary equilibria is crucial. To date, we have been getting our free-boundary equilibria from the EFIT and TEQ codes without much regard for the transport properties. An identification of the transport codes that can help us needs to be made, and interfaces from those codes to those of NIMROD will need to be defined. We also note that the preliminary transport studies have shown current extending beyond the separatrix. Allowance for current on the open fieldline could potentially help by allowing for more continuous gradients on our meshes.

ELM Milestone Progress Report
Second Quarter FY06
March 31, 2006

Q2 (March 31, 2006): Perform extended, linear perturbation studies to investigate the role of plasma edge density gradients. The density profiles will be used in spatially varying diffisivity coefficients, and they will be incorporated in extended-MHD effects. The shaping of the computational domain will also be improved to more accurately represent the DIII-D wall.

1.0 DIII-D Equilibria

Several equilibria based on DIII-D experimental shots 113207 and 113317 have been produced. Shot 113207 has higher density, pressure, and magnetic field that shot 113317. A comparison of the density and pressure profiles for the two shots is shown in Figures 1a,b. A cross-section of the equilibrium for shot 113317 is shown in Figure 2.

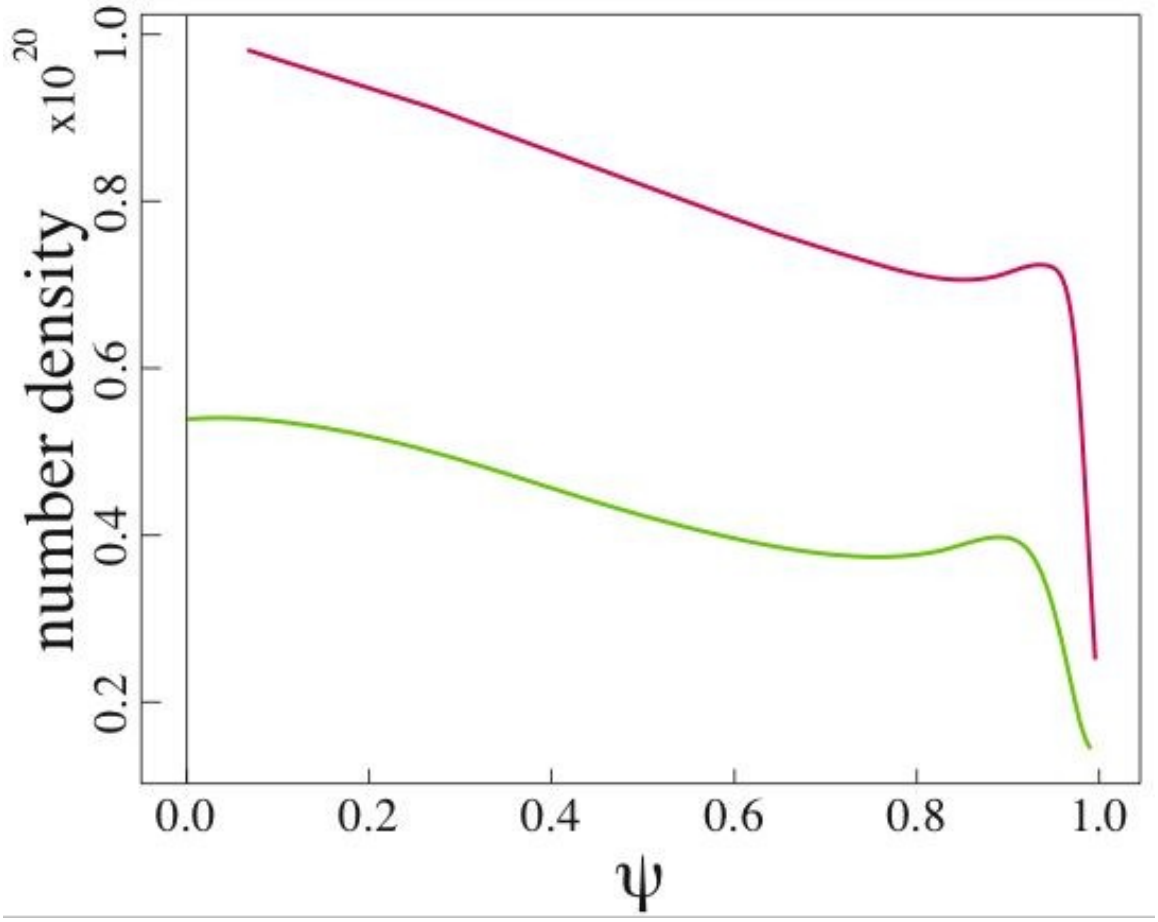

Figure 1a. Equilibrium density profiles for reconstructions of DIII-D shots 113207 (red) and 113317 (green).

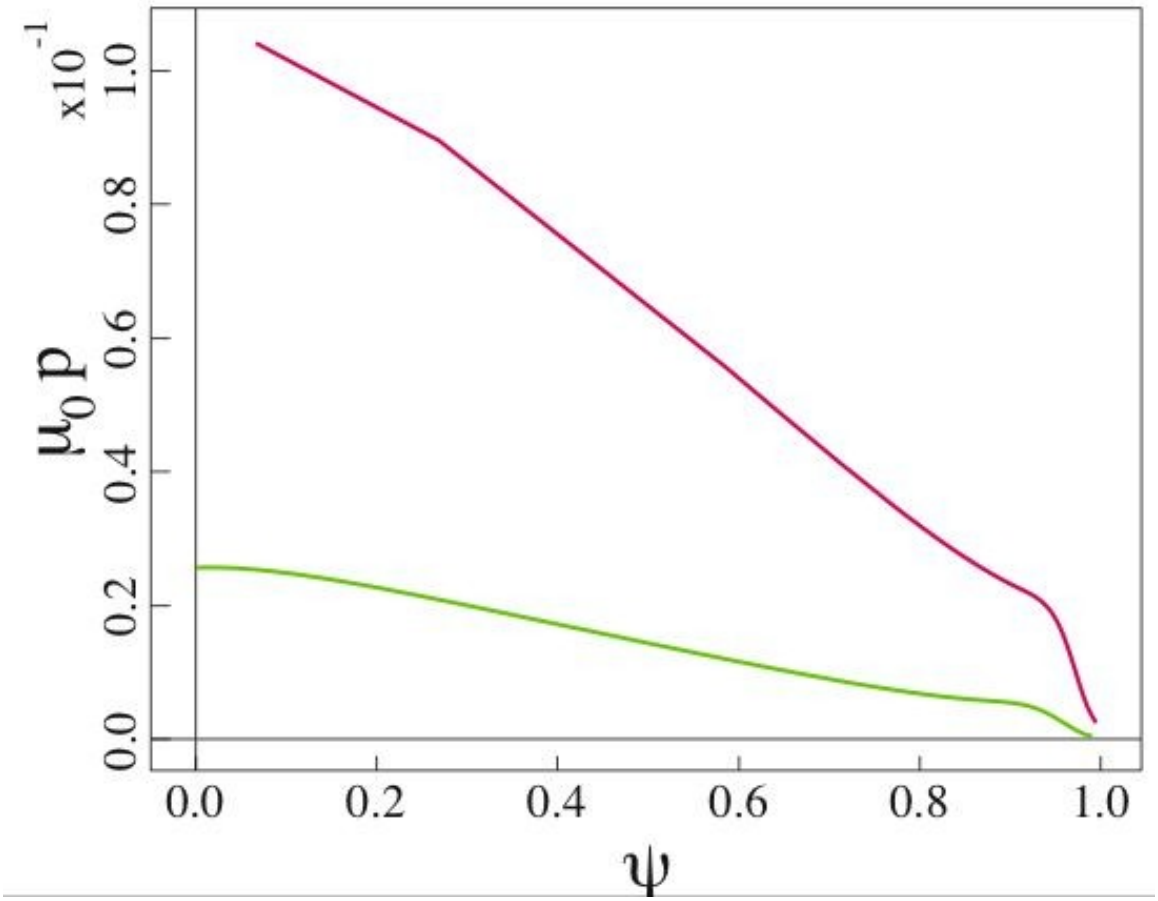

Figure 1b. Equilibrium pressure profiles for reconstructions of DIII-D shots 113207 (red) and 113317 (green).

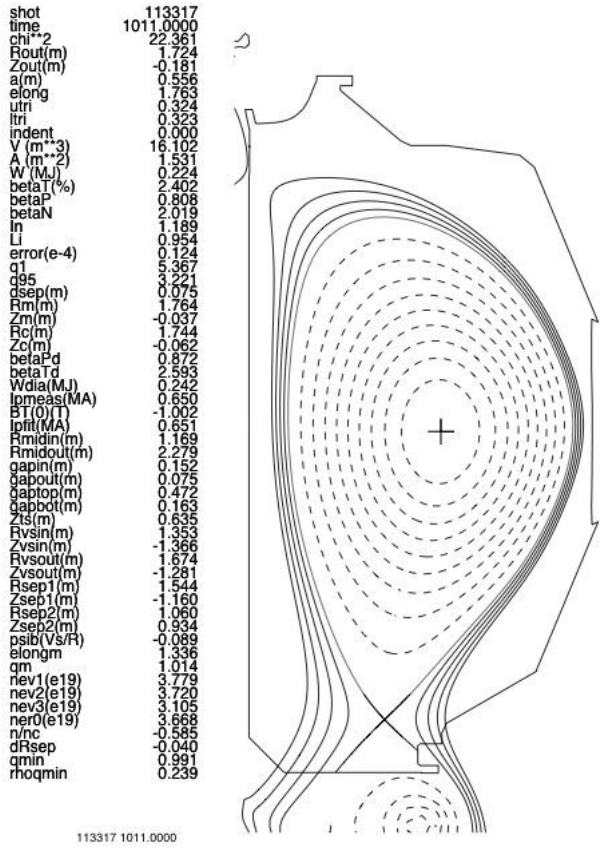

Figure 2. Poloidal cross section and parameters for shot 113317.

2.0 Linear and Non-linear Resistive MHD Studies

The linear stability and non-linear evolution of ELMs in these equilibria has been studied using the resistive MHD model in the NIMROD code. The time evolution of the kinetic energy in toroidal modes 1 through 43 is shown in Figure 3. The growth rate as a function of toroidal mode number n for this case is shown in Figure 4. The primary linearly unstable modes are in the range $5 < n < 25$, with exact details depending on the equilibrium (see Figure 4). Other modes are driven non-linearly, some by two wave interaction and some by three wave interaction (see Figure 4). The evolution of the temperature is shown in Figure 5.

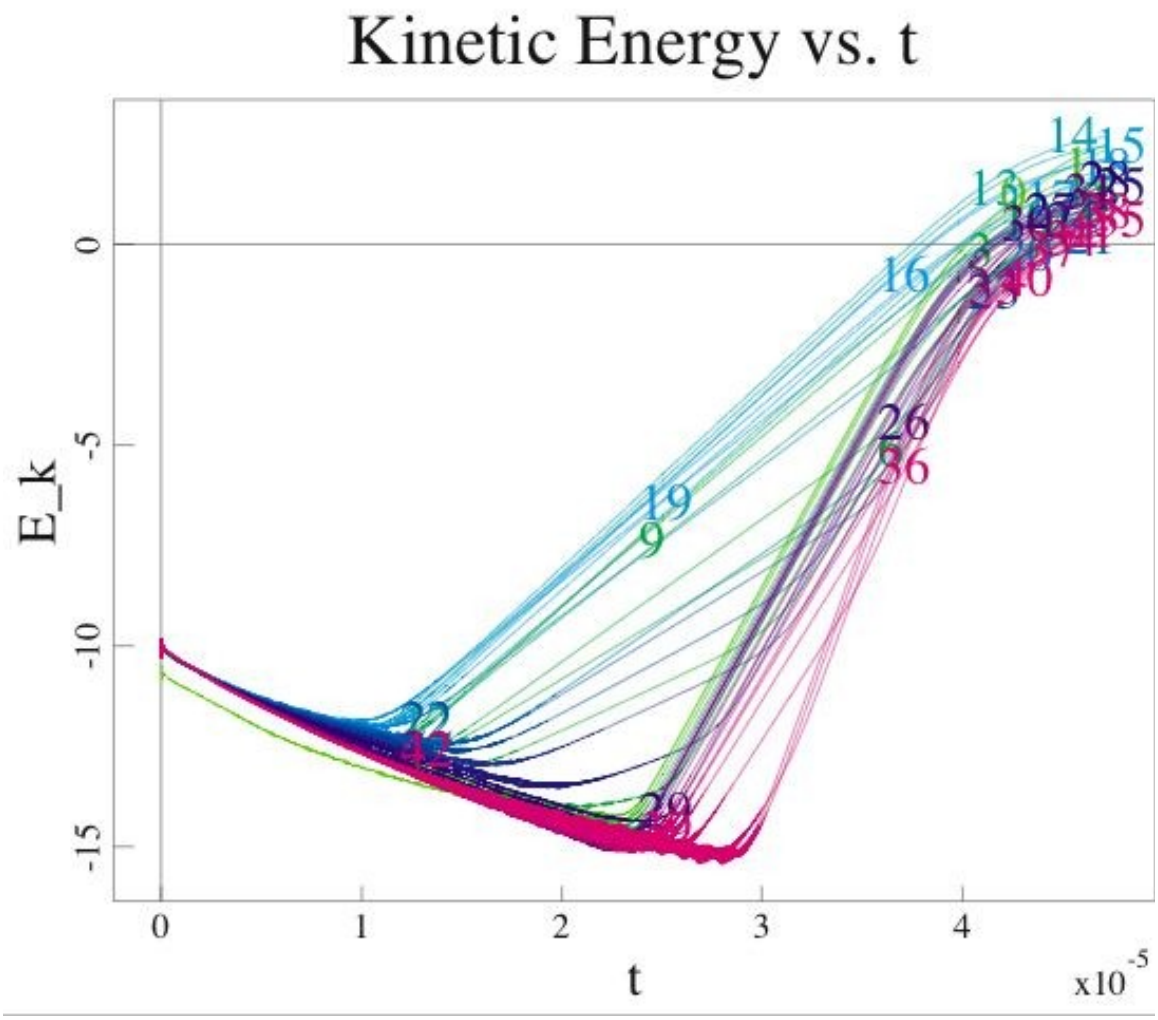

Figure 3. Kinetic energy in toroidal modes versus time for the non-linear evolution of shot 113207 using the resistive MHD model.

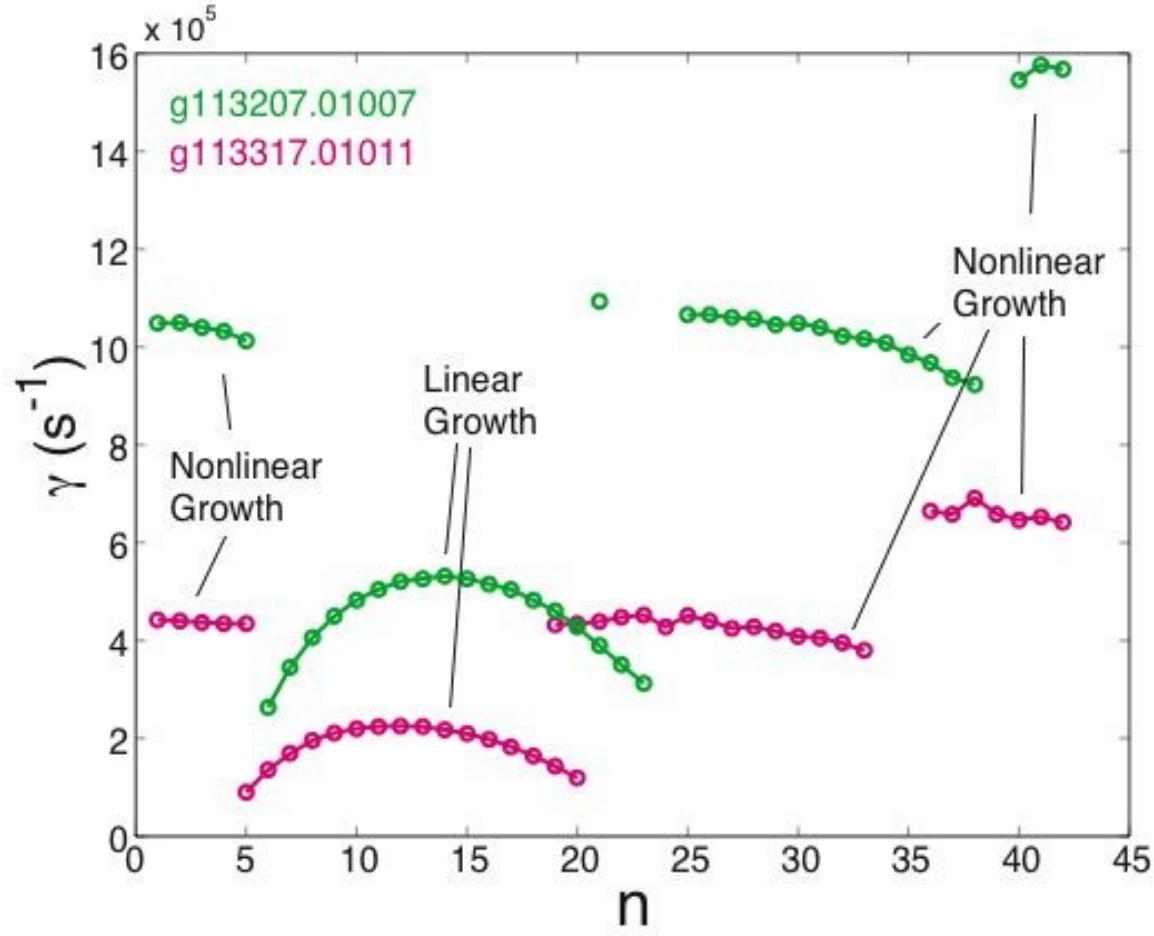

Figure 4. Growth rate versus toroidal mode number from the resistive MHD model for the two DIII-D equilibria under consideration. Linearly growing and non-linearly driven modes are identified.

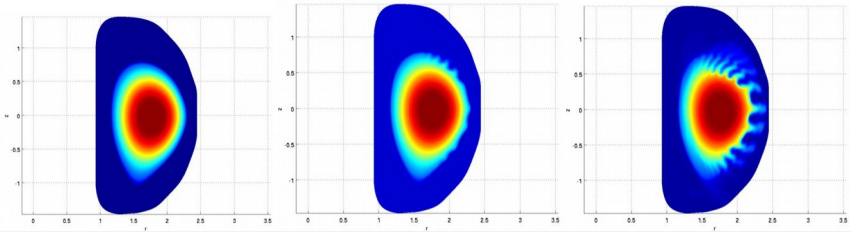

Figure 5. Evolution of the temperature during the non-linear evolution of an ELM in shot 113207.

3.0 Verification of the 2-fluid Model in NIMROD

The 2-fluid implementation in NIMROD has been validated against the ideal g-mode in a slab [K. V. Roberts and J. B. Taylor, Phys. Rev. Letters **8**, 197 (1962)]. Theory predicts two-fluid stabilization will occur when $\omega_* > 2\gamma_{MHD}$, where ω_* is the drift frequency and γ_{MHD} is the MHD growth rate. Results from the NIMROD code are in excellent agreement with this prediction, as seen in Figure 6. Verification of the gyro-viscosity on this problem is underway.

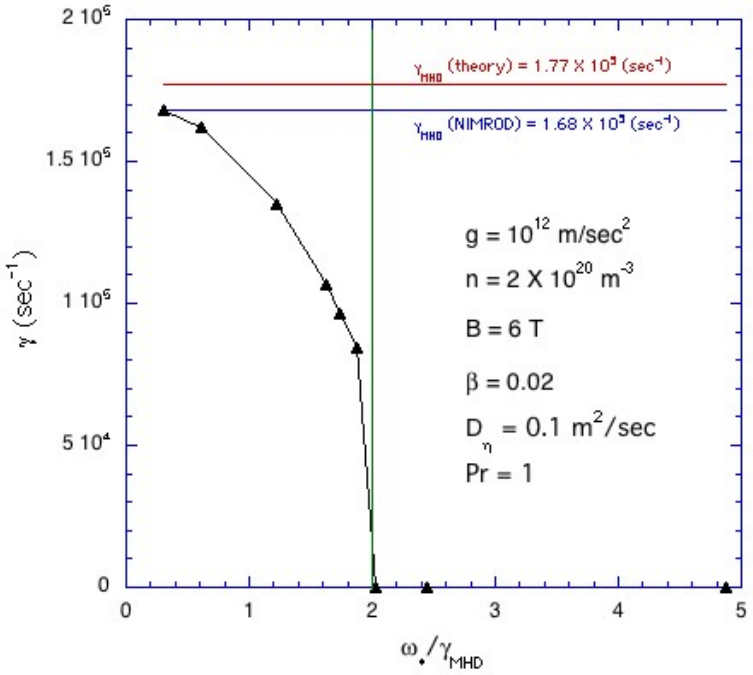

Figure 6. Growth rate of g-mode versus ω_* / γ_{MHD} with 2-fluid effects in the NIMROD code.

4.0 Stability of Model Equilibria with Edge Density Gradients

Model equilibria with paramaterized edge density gradients have been constructed. The density gradient can be shaped to match the equilibrium pressure profile according to $n_{eq}(R,\theta) = (1-\alpha_{v\tau})v_0 + \alpha_{v\tau}\Pi_{\varepsilon\theta}(P,\theta)/\Pi_0$. For the resistive MHD model, the growth rate has been determined for the $n = 13$ mode with the NIMROD code as functions of the pedestal particle density (normalized to peak density), and the parameter α_{nt}. The results are shown in Figures 7a,b.

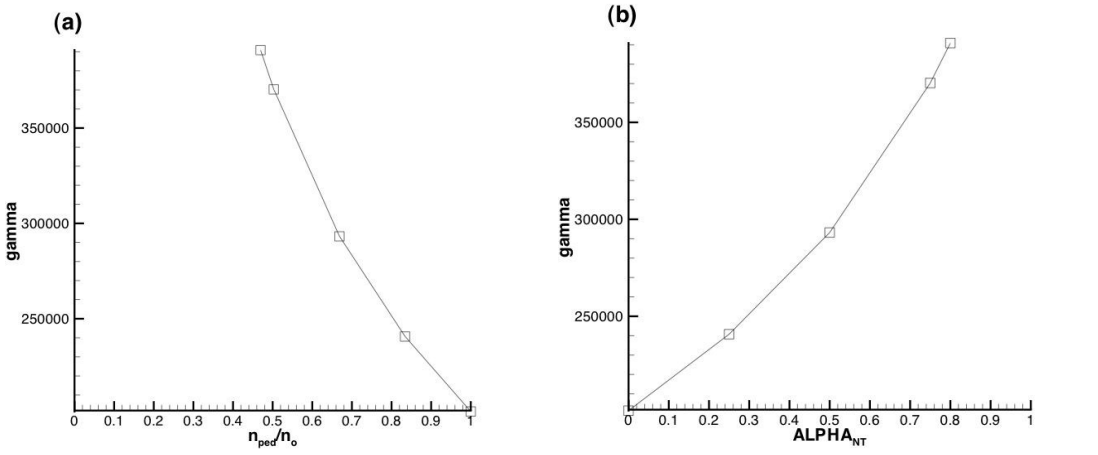

Figure 7. Linear growth rate for the $n = 13$ mode in the resistive MHD model for the generic equilibrium **a)** versus normalized pedestal density, and **b)** versus pedestal height.

Linear stability calculations have also been run for these equilibria using the 2-fluid model in NIMROD. These are shown in Figure 8. Note that the linear growth rate actually increases compared with the resistive MHD case (see Figure 7.)

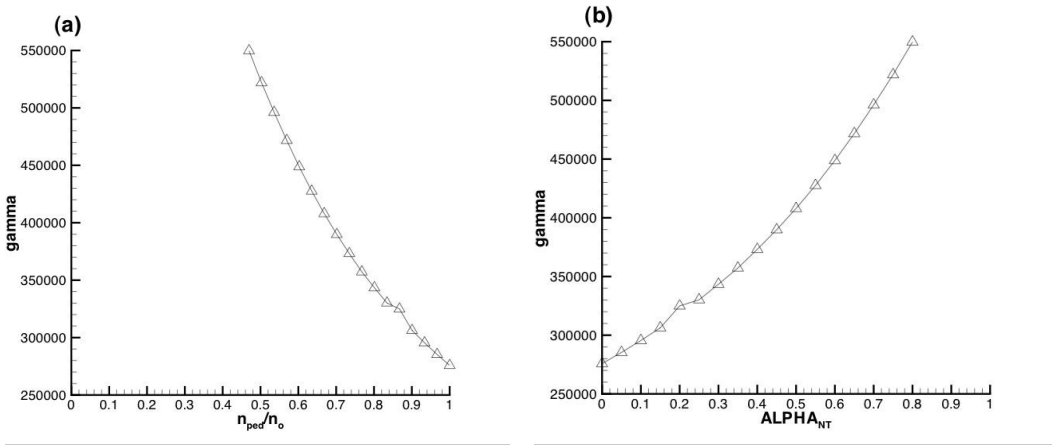

Figure 8. Linear growth rate for the $n = 13$ mode in the 2-fluid MHD model for the generic equilibrium **a)** versus normalized pedestal density, and **b)** versus pedestal height. The growth rate has increased compared with the resistive MHD result (see Figure 7.)